AN ABSORPTION REFRIGERATION SYSTEM USING IONIC LIQUID AND HYDROFLUOROCARBON WORKING FLUIDS

A Dissertation
Presented to
The Academic Faculty

By

Sarah Sungeun Kim

In Partial Fulfillment
Of the Requirements for the Degree
Doctor of Philosophy in the
School of Chemical & Biomolecular Engineering

Georgia Institute of Technology

May, 2014

AN ABSORPTION REFRIGERATION SYSTEM USING IONIC LIQUID AND HYDROFLUOROCARBON WORKING FLUIDS

Approved by:

Dr. Paul A. Kohl, Advisor
School of Chemical &Biomolecular Engineering
Georgia Institute of Technology

Dr. Yogendra K. Joshi
School of Mechanical Engineering
Georgia Institute of Technology

Dr. Andrei G. Fedorov
School of Mechanical Engineering
Georgia Institute of Technology

Dr. Thomas F. Fuller
School of Chemical &Biomolecular Engineering
Georgia Institute of Technology

Dr. Dennis W. Hess
School of Chemical &Biomolecular Engineering
Georgia Institute of Technology

Dr. Amyn S. Teja
School of Chemical &Biomolecular Engineering
Georgia Institute of Technology

Date Approved: November 27, 2013

In dedication to my loving parents

ACKNOWLEDGEMENTS

I would like to express my sincere gratitude to my thesis advisor, Prof. Paul Kohl. Without his advice, support, and encouragement, I would not have made it thus far. I would also like to thank my thesis committee members Prof. Yogendra Joshi, Prof. Andrei Fedorov, Prof. Tom Fuller, Prof. Dennis Hess, and Prof. Amyn Teja for their helpful input during my Ph.D. I would also like to give a very special thank you to all my current and past group members who have helped make my time at Georgia Tech such a wonderful experience. Thank you in particular to Daphne Perry and Johanna Stark for being such great friends. I would also like to thank Dr. Yoonjo Kim and my undergraduate research assistants Nishith Patel and Mark Evans for their assistance in computational work and running experiments. A special thank you goes out to Steven Isaacs for the chats and all the help he has given me every time I had a hard time working in the lab.

I would like to thank Dr. Hyea Kim for the friendship that has grown into a true sisterhood. Thank you to all of my Korean friends I have met in Atlanta for keeping me company during the time away from home and sharing my ups and downs.

Finally, I would like to thank my family who are my rock and foundation. Thank you for all the love and sacrifices and for always believing in me.

TABLE OF CONTENTS

LIST OF TABLES

LIST OF FIGURES

LIST OF SYMBOLS

A	Coefficients in Lockhart and Martinelli correlation
B_1	Second virial coefficient [cm^3/mol]
C	Heat capacity rate [J/K·s]
CE	Cooling-to-total-energy
CE_{Th}	Cooling-to-total-thermal energy
COP	Coefficient of performance
C_p	Specific heat [J/kg·K]
d_h	Hydraulic diameter [m]
F	Adjustable binary interaction parameter
f	Fanning friction factor
G	Gibbs energy [J]
G_m	Mass flux [kg/m^2s]
H	Enthalpy [J]
h	Specific enthalpy [J/kg]
HX	Heat exchanger
k	Adjustable binary interaction parameter
l	Adjustable binary interaction parameter
M	Molecular weight [kg/mol]
m	Mass flow rate [kg/s]
P	Pressure [MPa]
P_c	Critical Pressure [MPa]

Q	Heat transfer rate [W]
R	Gas constant, 8.314 J/mol·K
Re_{lo}	Liquid-only Reynolds number
S	Entropy [J/K]
s	Specific entropy [J/kg·K]
T	Temperature [K]
T_c	Critical Temperature [K]
V	Molar volume [cm^3/mol]
$\tilde{V}$	Saturated molar liquid volume [cm^3/mol]
v	Specific volume [m^3/kg]
We_{lo}	Liquid-only Weber number
W_p	Pumping work [W]
X	Martinelli parameter
x	Liquid phase refrigerant mole fraction
x^m	Liquid phase refrigerant mass fraction
x_n	Liquid phase ionic-liquid mole fraction
x^v	Vapor quality
z	Coordinate [m]

Greek symbols

α	Circulation ratio
β	Equation of state constant
γ	Activity coefficient
δ	Aspect ratio

ε	Solution heat exchanger efficiency
η	System efficiency utilizing waste heat
μ	Viscosity [Pa·s]
ρ	Density [kg/m^3]
τ	Adjustable binary interaction parameter [K]
Φ	Fugacity coefficient
φ	Two-phase multiplier
ψ	Void fraction

Subscripts

0	Reference state
1, ., 10	State numbers indicated in the absorption refrigeration system diagram
a	Absorber
c	Condenser
d	Desorber
e	Evaporator
IL	Ionic-liquid
l	Liquid
r	Refrigerant
s	Strong-ionic liquid solution
shx	Solution heat exchanger
v	Vapor
w	Weak-ionic liquid solution

Superscripts

E	Excess property
id	Ideal solution
ig	Ideal gas
R	Residual property
s	Saturation

SUMMARY

Efficient heat management in energy intensive applications such as server and data centers has become a national concern due to the magnitude of the energy consumed. In that matter, the absorption refrigeration system is an attractive solution because the abundant waste heat available in the data centers can be recycled to run the heat pump, which will bring about significant cooling cost savings. Cooling in data centers typically take up to 30 to 50% of the total costs. The use of absorption refrigeration has been limited due to the drawbacks related to the working fluids in commercially available equipment. Recently, ionic liquids (ILs) have been suggested as the absorbent in absorption heat pumps due to their tunable properties, negligible volatility and high thermal stability.

The non-random-two-liquid-model was initially used to analyze the feasibility of the new IL based working fluid. Hydrofluorocarbons (HFCs) were paired with IL absorbents due to their good properties as refrigerants. The cooling-to-total-energy (CE) efficiency had a local maximum with respect to desorber temperature due to the solubility limit at lower temperatures and large heating requirements at higher temperatures. The waste heat recycling coefficient of performance (COP) continually increased with respect to desorber temperature and among the HFCs studied in this work, R134 gave the highest COP value, which is up to 40 times higher than that of typical vapor compression systems and 60 times higher than NH_3/H_2O and H_2O/LiBr absorption refrigeration systems.

A cubic equation of state, Redlich-Kwong equation of state (RK-EOS), was employed for accurate computation of mixture properties over a wide range of operating

conditions. Analysis using the RK-EOS model showed that the CE trend in refrigerants followed the trend of solubility in the [bmim][PF_6] IL. However, the trend in COP was different from that of CE as the operating pressure ranges became an important factor. Required pumping work of the working fluids has also been analyzed using a two phase pressure drop equation and the results show that the impact of viscous IL flow is insignificant compared to the total pumping work.

The HFCs studied in this work have very similar structures, which are in the form of either fluoromethane or fluoroethane. However, the extent of solubility and system efficiency in the same IL, [bmim][PF_6], made a large difference. Most surprisingly, even when the refrigerant had the same chemical formula, the change in fluorine position in tetrafluoroethane showed significantly different system performance. The symmetrical tetrafluoroethane had superior CE and COP over the asymmetrical tetrafluoroethane most likely due to the higher probability to form hydrogen bonding with the absorbent. The computational results for various HFC/IL pairs show that in selecting the working fluid pairs, the refrigerant should have high overall solubility in the IL and a large gradient of solubility with respect to temperature. Also, refrigerants with small pressure ranges are preferred.

In addition to the simulation study, a bench-top absorption refrigeration system was built and operated using IL based working fluids for the first time. The effect of cooling was observed by operating the test system. The experimental results were congruent with the predictions from the modeling work. In conclusion, an absorption refrigeration system based on the IL chemical compressor has been shown to be a

promising solution in applications which need efficient cooling and generate abundant waste heat.

CHAPTER 1

INTRODUCTION

Over the last decade, the energy consumption of large scale information technology equipment and infrastructure has grown into a national concern due to the high demand for data computing and storage capacity. The Environmental Protection Agency reported that the energy consumption of servers and data centers in 2006 was more than double that consumed in year 2000[1]. In fact, data centers can be more than 40 times as energy intensive as conventional office buildings[2]. A grand challenge in future high performance computing and data storage systems is to find economical ways to recover and recycle low-quality waste heat, in order to partially offset the enormous energy needs for infrastructure cooling. Cooling is one of the major factors in total energy consumption in data centers accounting for about 30%-50% of the total power drawn from the grid[3].

Toward this end, the absorption refrigeration cycle is of interest as a means of utilizing low-quality waste heat. Absorption chillers offer an opportunity to recycle large amounts of industrial waste heat[4]. Also, renewable energy sources which generate heat can be directly used for refrigeration without the need of conversion to electrical power[5]. However, the use of the absorption refrigeration cycle has been somewhat limited due to technological challenges, health hazards, and environmental concerns of existing systems[6].

Recently, ionic liquids (ILs), liquid salts at ambient temperature, have been suggested as an alternative absorbent replacing the previous working fluids in absorption

refrigerant systems[7]. However, due to the large number of ionic liquids, possibly about 10^{18} cation/anion combinations[8], a set of criteria is required to screen out suitable candidates for absorption heat pump applications.

The goal of this work was to demonstrate and model the feasibility of a new absorption refrigeration cycle based on newly available non-volatile absorbents to scavenge waste heat and convert it into useful cooling with possibly little added energy. Theoretical and experimental studies have been conducted to understand the features of the new working fluids to provide guidance in the operation and efficiency of IL-based absorption refrigeration systems.

CHAPTER 2

BACKGROUND

2.1 Overview of Absorption Refrigeration System

Absorption heat pumps are mainly consisted of an absorber, desorber/generator, condenser, evaporator, and a liquid pump. Unlike the vapor compression system, where one refrigerant or mixture of refrigerants can be used in the cycle, the working fluid in an absorption heat pump is a binary solution consisting of refrigerant and absorbent.

2.1.1 Ammonia/Water Working Fluid

Ammonia refrigerant and water absorbent systems have been in use since the mid-1800s, originally for refrigeration[9]. Since the 1970s they are under consideration for residential and commercial heating and cooling[10]. Ammonia and water have high affinity, which is beneficial as working fluid pairs. However, Ammonia is a toxic and explosive substance that limits the usage for indoor use. Also the vapor pressure of water is not negligible relative to that of ammonia. As a consequence, a rectifier at the exit of the generator is required for post-desorption separation of the fluid streams, Figure 2.1. Typical high operating temperatures are between 120 and 132°C with an approximate system efficiency of 0.9[10].

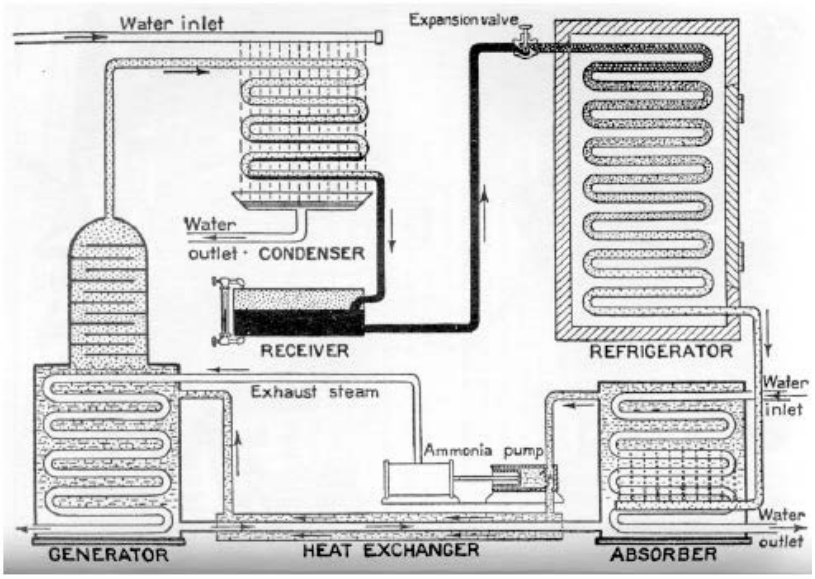

Figure 2.1: An ammonia absorption cycle[9,11].

2.1.2 Water/Lithium Bromide Working Fluid

The use of water/LiBr for absorption refrigeration systems began around 1930[5,12]. Two outstanding features include the non-volatility of LiBr absorbent (elimination of rectifier) and the high heat of vaporization of water as a refrigerant. However, precipitates form when the mass fraction of the salt LiBr exceeds the solubility limit. This crystallization of LiBr can block the system components and shorten the life time of the equipment. Due to the use of water as the refrigerant, cooling is limited to temperatures higher than 0°C and the system is operated at sub-atmospheric conditions. For an evaporator temperature of 5°C, the corresponding vapor pressure of water is 0.009 atm. Therefore, the equipment needs to be hermetically sealed. The aqueous LiBr itself is highly aggressive to many metals including carbon steel and copper in the presence of dissolved oxygen[10]. Typical high operating temperatures are between 120 and 170°C with an approximate system efficiency ranging between 0.9 and 1.3[10].

2.1.3 Ionic Liquid Based Working Fluids

Ammonia/water and water/LiBr working fluids are most commonly used in commercial absorption cooling cycles. However continuous efforts have been made to replace these fluids due to the several aforementioned drawbacks. Among the new working fluids, the IL based working fluids have drawn significant attention[7].

ILs are a liquid salt at ambient temperature usually composed of organic cations and inorganic anions. ILs have the character of molten salts, which are moisture and air stable at room temperature. Most ILs are thermally stable to temperatures well above those in vapor compression refrigeration systems, > 400K[13–17]. However, in the case of a prolonged exposure to elevated temperatures, the effective decomposition temperature could be lower. Blake et al.[17] reported that the half-life of 1-butyl-3-methylimidazolium hexafluorophosphate ([bmim][PF_6]) is only 138 days at 573K, while at 423K (the highest operating temperature of an absorption system), it could be more than 10 years. Due to the toxic and flammable nature of volatile organic compounds(VOCs) [18], ILs with the negligible vapor pressure are considered to be green solvents and possible replacements of solvents for organic synthesis[8], biphasic catalysis, separation and extraction processes[19], and dissolution of biomaterials[20]. Note that although ILs are 'non-flammable', some of ILs could be 'combustible' at sufficiently high temperature (near their decomposition temperature) upon exposure to fire or combustion[21]. Also, Jastorff et al.[22] found the toxicity of the various ILs spanned a range of about 1000× (from least to most toxic) based on the toxicological tests of a series of ILs with imidazolium cations and [PF_6^-], [BF_4^-], [Cl^-], [Br^-] and tosylate anions. However, even the most toxic of the

ILs has about the same toxicity as the least toxic of four common organic solvents (methanol, acetone, acetonitrile, MTBE) that were tested using the same protocol[15]. Thus, even though some ILs may not be intrinsically "green", they can be designed to be environmentally benign, with large potential benefits for sustainable chemistry[23]. While the chemistry of ILs and their utilization for chemical processes have been reported in many publications, solubility data with other solvents and thermodynamic properties of mixtures containing ILs and possible refrigerants are less common[13].

With the above mentioned features of ILs such as tunable properties, zero vapor pressure, and high thermal stability, ILs are promising absorbents in absorption heat pumps. In particular, the low volatility of the IL enables easy separation of the volatile working fluid from the IL by thermal stratification with the minimum harmful impacts on environment. Since many ILs have their melting points below the lowest solution temperature in absorption system (~300K)[24–28], they also eliminate the crystallization and metal-compatibility problems of the water/LiBr system. In this study ILs are used as an absorbent fluid in a miniature absorption refrigeration system designed for current electronic cooling requirements (i.e., benchmark 100 W/cm^2 power dissipation and 85^oC chip temperature).

In this study, hydrofluorocarbon (HFC) refrigerants were paired with ILs for the absorption refrigeration cycle. HFCs are commonly used refrigerants in vapor compression systems due to their moderate pressure ranges and high heat of vaporization. The REFPROP 6.0 software, developed by the National Institute of Standards and Technology, has been used to calculate the thermodynamic and transport properties of the pure HFC refrigerants. It implements three models for the thermodynamic properties of

pure fluids[29]: (i) equations of state explicit in the Helmholtz energy, (ii) the modified Benedict-Webb-Rubin equation of state, and (iii) an extended corresponding states (ECS) model.

2.2 Overall Description of the Cycle

The principal features of the absorption refrigeration cycle are shown in Figure 2.2. The cycle resembles that of the vapor compression refrigeration system, except the vapor compressor is replaced with a thermochemical process consisting of an absorber, a liquid pump, a solution heat exchanger, a desorber, and an expansion device. The pressurization in the thermochemical process starts in the absorber, where the refrigerant vapor from the evaporator (state point 2) is exothermically absorbed into the strong-IL solution (state point 10), resulting in a weak IL solution at state point 5. The IL solution is pressurized by the liquid pump after the absorber. Then, the solution (regenerative) heat exchanger preheats the weak-IL solution at state point 6 creating state point 7 using heat from the strong-IL solution flowing back to the absorber (from the desorber). In the desorber, high pressure and high temperature superheated refrigerant vapor is released from the IL via desorption from the weak-IL solution by the addition of heat (preferably high quality waste heat). The strong-IL returns to the absorber through the solution heat exchanger and an expansion device. The condensation/absorption process at the absorber and vaporization/desorption process at the desorber both occur in the liquid phase. This allows use of a liquid pump to create the pressure difference between condenser and evaporator. Although the presence of the absorber and desorber increases the overall system volume, the displacement volume and power consumption for liquid compression

are much smaller than those for vapor compression. Table 2.1 summarizes the main components/processes of an absorption heat pump system using IL/refrigerant mixture as a working fluid.

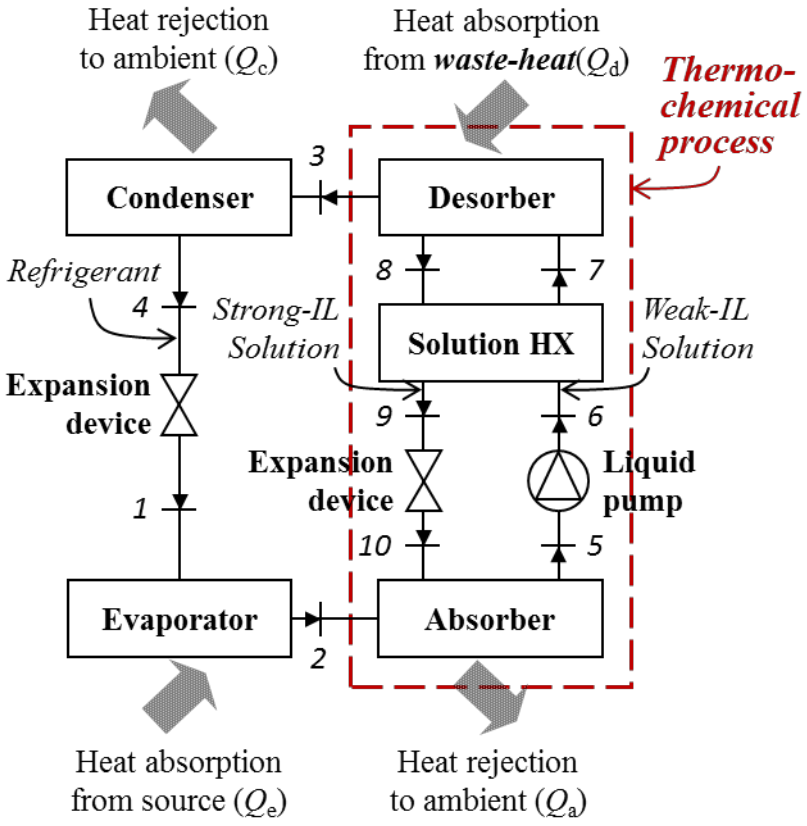

Figure 2.2: Schematic diagram of an absorption refrigeration system.

Table 2.1: Main components and the processes of an absorption refrigeration system using IL/refrigerant as working fluids.

Component	**State**	**Process**
Evaporator	$1 \rightarrow 2$	Heat absorption from target
Absorber	$2, 10 \rightarrow 5$	Refrigerant absorption /condensation into IL
Pump	$5 \rightarrow 6$	Isentropic pressurization
Solution HX	$6 \rightarrow 7, 8 \rightarrow 9$	Regenerative pre-heating
Desorber	$7 \rightarrow 8, 3$	Refrigerant desorption/vaporization from IL
Condenser	$3 \rightarrow 4$	Heat rejection to ambient
Expansion device	$4 \rightarrow 1, 9 \rightarrow 10$	Isenthalpic expansion

In this work, system-level simulations of refrigerant/absorbent combinations have been carried out. Energy and mass conservation equations for all components comprising the system were simultaneously solved to determine the heat and workloads. The overall energy balance for the system is given by

$$Q_d + Q_e + W_p = Q_c + Q_a \tag{2.1}$$

where W_p is the liquid pump work and Q is the heat input/output. The subscripts d, e, c, and a represent the desorber, evaporator, condenser, and absorber, respectively. All values of heat are expressed as positive (magnitude) values regardless of the direction (in or out) of heat flow.

A counter-flow type heat exchanger was used to recover heat from the strong-IL solution and to reduce the heat supply to the desorber (Q_d). One stream in the counter-flow heat exchanger can undergo a greater temperature change than the other due to unequal heat capacity values and mass flow rates for the weak and strong streams. The

heat capacity rate is defined by Equation 2.2 and can be used to determine which stream will limit the amount of heat transfer[30].

$$C = mC_p \tag{2.2}$$

C is the heat capacity rate, m is the mass flow rate, and C_p is the heat capacity. The heat capacity rates, C_{hot} and C_{cold}, can be calculated for both inlet streams by Equations 2.3 and 2.4.

$$C_{hot} = m_{hot}C_{p,hot} \tag{2.3}$$

$$C_{cold} = m_{cold}C_{p,cold} \tag{2.4}$$

The heat transfer is limited by the minimum value of the two heat capacity rates.

$$C_{\min} = \begin{cases} C_{hot}, & C_{hot} \le C_{cold} \\ C_{cold}, & C_{cold} < C_{hot} \end{cases} \tag{2.5}$$

The maximum possible heat transfer possible for an adiabatic, infinitely long counter-flow heat exchanger is given by Equation 2.6.

$$Q_{\max} = C_{\min}(T_{hot,in} - T_{cold,in}) \tag{2.6}$$

However, a real heat exchanger can only achieve a fraction of the maximum heat transfer possible depending on its efficiency, ε, Equation 2.7.

$$Q_{actual} = \varepsilon Q_{\max}, 0 \le \varepsilon \le 1 \tag{2.7}$$

This estimate of the heat transfer at the counter-flow heat exchanger can then be used to determine the temperature and enthalpy of the exit streams of the solution heat exchanger.

The energy conservation for a sub-system consisting of a regenerative heat exchanger and a pump is given by Equation 2.8.

$$(h_9 - h_8)(m_w - m_r) = (h_7 - h_5)m_w - W_p \tag{2.8}$$

In Equation 2.8, h is specific enthalpy and the subscripts correspond to the locations shown in the system diagram, Figure 2.2. Also, m_w and m_r are the mass flow rates of the weak-IL solution and refrigerant leaving the desorber, respectively. Energy conservation for the desorber is given by Equation 2.9.

$$Q_d = h_8\left(m_w - m_r\right) + h_3 m_r - h_7 m_w \tag{2.9}$$

Similarly, heat rejected at the absorber is given by Equation 2.10.

$$Q_a = h_5 m_w - h_{10}\left(m_w - m_r\right) - h_2 m_r \tag{2.10}$$

Energy conservation for the condenser and the evaporator yield the respective heat loads, Equations 2.11 and 2.12.

$$Q_c = \left(h_4 - h_3\right) m_r \tag{2.11}$$

$$Q_e = \left(h_2 - h_1\right) m_r \tag{2.12}$$

The cooling-to-total-energy (CE) is then defined as the heat removed at the evaporator divided by the power supplied to the desorber and the pump, Equation 2.13.

$$CE = \frac{Q_e}{Q_d + W_p} \tag{2.13}$$

Since waste heat is intended to be used to heat the desorber, the practical coefficient of performance (COP), η, is defined by Equation 2.14.

$$\eta = \frac{Q_e}{W_p} \tag{2.14}$$

Equation 2.14 is the usual figure of merit for absorption refrigeration/heat pump systems where waste heat is used.

CHAPTER 3

THERMODYNAMIC MODEL OF THE CYCLE

3.1 Theoretical Models Used in System Analysis

The initial two sections of this chapter present two general procedures for computing the vapor liquid equilibrium (VLE).

3.1.1 Non-Random-Two-Liquid Model

In general, the VLE at low and medium pressure for an N-component system can be described by Equation 3.1[31].

$$x_i \gamma_i P_i^s = y_i P \Phi_i \quad (i = 1, ..., N) \tag{3.1}$$

In Equation 3.1, x is the liquid-phase mole fraction, γ is the activity coefficient, P^s is the saturated vapor pressure, y is the vapor-phase mole fraction, P is the system pressure, and Φ is the fugacity coefficient. Subscript i indicates the corresponding species.

At the temperatures of interest here, which is lower than the IL decomposition temperature, for gas (1)/ionic liquid (2) binary mixtures, it is reasonable to neglect the ionic liquid in the vapor phase; $y_1 = 1$. Then, the activity coefficient for species 1 is given by Equation 3.2[31].

$$\gamma_1 = \frac{P \Phi_1}{x_1 P_1^s} \tag{3.2}$$

The correlations of the refrigerant (1)/IL (2) mixture properties were developed based on the non-random two-liquid (NRTL) activity coefficient model by Shiflett and Yokozeki[32]. This model was used in this study for preliminary analysis of various working fluids, Equations 3.3 and 3.4.

$$\ln \gamma_1 = x_2^2 \left[\tau_{21} \left(\frac{F_{21}}{x_1 + x_2 F_{21}} \right)^2 + \frac{\tau_{21} F_{21}}{\left(x_2 + x_1 F_{12} \right)^2} \right] \tag{3.3}$$

$$\ln \gamma_2 = x_1^2 \left[\tau_{12} \left(\frac{F_{12}}{x_2 + x_1 F_{12}} \right)^2 + \frac{\tau_{12} F_{12}}{\left(x_1 + x_2 F_{21} \right)^2} \right] \tag{3.4}$$

Parameter *F* is determined by an adjustable binary interaction parameter τ, Equations 3.5 and 3.6.

$$F_{12} \equiv \exp\left(-0.2\tau_{12}\right) \quad \text{and} \quad F_{21} \equiv \exp\left(-0.2\tau_{21}\right) \tag{3.5}$$

$$\tau_{12} \equiv \tau_{12}^0 + \frac{\tau_{12}^1}{T} \quad \text{and} \quad \tau_{21} \equiv \tau_{21}^0 + \frac{\tau_{21}^1}{T} \tag{3.6}$$

T is absolute temperature. The parameters, τ_{12}^0, τ_{12}^1, τ_{21}^0, and τ_{21}^1, have been determined based on literature VLE data.

The fugacity coefficient of species 1 can be computed by Equation 3.7.

$$\Phi_1 = \exp\left[\frac{(B_1 - \tilde{V}_1)(P - P_1^s)}{RT} \right] \tag{3.7}$$

B is the second virial coefficient[33], $\tilde{V}$ is the saturated molar liquid volume, and R is the universal gas constant.

Then, the mixture enthalpy, *H*, was calculated from Equation 3.8.

$$H = H^{id} + H^E \tag{3.8}$$

The ideal solution property of enthalpy, H^{id}, in Equation 3.8 can be obtained from Equation 3.9 for a binary system.

$$H^{id} = x_1 H_1 + x_2 H_2 \tag{3.9}$$

The specific enthalpy, h_{IL}, of ILs were calculated using Equation 3.10[31].

$$h_{IL} = \int_{T_0}^{T} c_{p,IL}\, dT + \int_{P_0}^{P} v_{IL}\, dP + h_0 \tag{3.10}$$

In Equation 3.10, $c_{p,IL}$ and v_{IL} are the specific heat and specific volume of the IL, respectively. The IIR (International Institute of Refrigeration) reference state was adopted; $h_0 = 200$ kJ/kg for the saturated liquid at $T_0 = 0^{\circ}\mathrm{C}$ ($P_0 = P_{sat}(T_0)$).

The excess enthalpy, H^E, can be calculated from Equation 3.12[32].

$$H^E = -RT^2 \left[x_1 \left(\frac{\partial \ln \gamma_1}{\partial T} \right)_{P,x} + x_2 \left(\frac{\partial \ln \gamma_2}{\partial T} \right)_{P,x} \right] \tag{3.12}$$

3.1.2 Redlich-Kwong Equation of State

A more general model than the NRTL model is the cubic equations of state, which can also be used in high pressure VLE conditions. In this work the Redlich-Kwong equation of state (RK-EOS) was chosen to calculate the thermodynamic properties of the fluids. The RK-EOS was selected due to the relative simplicity of the formulation and presence of a temperature attraction term as the affinity between the refrigerant and absorbent greatly depend on temperature. Binary interaction parameters were introduced to improve the accuracy of the model. Several assumptions were made in the calculations: (1) the expansion process was isenthalpic; (2) the compression process was isentropic; (3) state 4 was a saturated liquid refrigerant; (4) state 2 was a saturated vapor

refrigerant; (5) the vapor quality at state 5 was zero. The corresponding state numbers are shown in Figure 2.2.

The RK-EOS can be written in the following form, Equations 3.15-17[31].

$$P = \frac{RT}{V-b} - \frac{a(T)}{V(V+b)} \tag{3.15}$$

$$a(T) = 0.42748\frac{R^2T_c^2}{P_c}\left[\sum_{k=0}^{\leq 3}\beta_k(1/T_r - T_r)^k\right],\ T_r \equiv T/T_c \tag{3.16}$$

$$b = 0.08664\frac{RT_c}{P_c} \tag{3.17}$$

In Equations 3.15 to 3.17, V is the molar volume, a and b are constants, and T_c and P_c represents the critical temperature and pressure, respectively. The parameters β_k in the temperature dependent function of Equation 3.16 were determined so as to yield the vapor pressure of each pure compound, the refrigerant and the ionic liquid alone[34]. The vapor pressure of ionic liquid is practically zero and data for the critical parameters (T_c and P_c) are not available. An estimate of the critical constants based on liquid densities alone is generally sufficient for correlating the solubility data of high boiling-point compounds (ILs) at the operating conditions[35]. However, the temperature dependent part of the absorbent is important for the interaction of the refrigerantand absorbent. Therefore, β for the absorbent was modeled by two terms and treated as an adjustable fitting parameter for the mixture.

Three binary interaction parameters (BIPs), τ, l, and k were introduced in the a and b parameters for N component mixtures[36].

$$a = \sum_{i,j=1}^{N} \sqrt{a_i a_j}(1+\tau_{ij}/T)(1-l_{ij})x_i x_j,\ a_i = 0.42748\frac{R^2 T_{ci}^2}{P_{ci}}\left[\sum_{k=0}^{\leq 3}\beta_k (1/T_r - T_r)^k\right] \quad (3.19)$$

$$b = \frac{1}{2}\sum_{i,j=1}^{N}\left(b_i + b_j\right)(1-l_{ij})(1-k_{ij})x_i x_j,\ b_i = 0.08664\frac{RT_{ci}}{P_{ci}} \quad (3.21)$$

Also, the following relationships exist: $\tau_{ij} = \tau_{ji}; l_{ij} = l_{ji}; k_{ij} = k_{ji};\ \tau_{ii} = l_{ii} = k_{ii} = 0$.

VLE for a two component system can be obtained by solving equilibrium conditions, Equation 3.22, where x_i is the liquid phase mole fraction of the *i*-th species, y_i is the vapor phase mole fractions of the *i*-th species, and ϕ_i is the fugacity coefficient of the *i*-th species.

$$x_i \phi_i^l = y_i \phi_i^v \quad (3.22)$$

The fugacity coefficient can be calculated from Equations 3.23 and 3.24[36].

$$\ln \phi_i = \int_V^\infty \left\{\left(\frac{\partial(nZ)}{\partial n_i}\right)_{T,nV,n_j} - 1\right\}\frac{dV}{V} - \ln Z \quad (3.23)$$

$$Z = \frac{PV}{RT} \quad (3.24)$$

The equilibrium condition, Equation 3.22, is used to compute the solubility of a refrigerant in an IL at a given temperature and pressure. An iterative computational code was used to find the BIPs for each binary working fluid mixture of a refrigerant and IL. The objective function was to minimize the non-linear least square difference between the computed pressure and measured pressure value with the equilibrium condition (Equation 3.22) used as a constraint. The BIPs found were used to compute solubility values at different temperature and pressure conditions.

The EOS was then used to find the enthalpy values at the point of interest, Equation 3.25.

$$H = H^R + \int_{T_0}^{T} \sum_{i=1}^{N} x_i C_{pi}^{ig} dT + H_0 \tag{3.25}$$

The ideal-gas heat capacity of the i-th species, C_{pi}^{ig}, is modeled in Equation 3.26.

$$C_{pi}^{ig} = C_{pi}^{0} + C_{pi}^{1} T + C_{pi}^{2} T^2 + C_{pi}^{3} T^3 \tag{3.26}$$

The residual enthalpy of the mixture, H^R, can be calculated using the residual Gibbs energy, G^R, Equations 3.27 and 3.28.

$$\frac{G^R}{RT} = \int_o^P (Z-1)\frac{dP}{P} \tag{3.27}$$

$$H^R = -RT^2 \left[\frac{\partial (G^R / RT)}{\partial T} \right]_P \tag{3.28}$$

Using the heat capacity and residual enthalpy for each species in the mixture, the enthalpy for the RK-EOS is given by Equation 3.29.

$$H = \left(\frac{a}{b} - \frac{T}{b}\frac{da}{dT} \right) \ln \frac{V}{V+b} + RT(Z-1) + \int_{T_0}^{T} \sum_{i=1}^{N} x_i C_{pi}^{ig} dT + H_0 \tag{3.29}$$

3.2 Two Phase Pressure Drop Model

The viscosity of ILs are often relatively high; for example, the viscosity of [bmim][PF_6] at 294K and atmospheric pressure is 376 mPa·s[37]. Thus, the IL flow in microchannels used in the absorber and desorber may create large pressure drops, which can affect the system performance. The average pressure drop through the microfluidic

channel heat exchangers was evaluated using a two-phase pressure drop equation[38,39], Equation 3.28.

$$-\left(\frac{dP}{dz}\right)=\left[\frac{2f_{\mathrm{l}}G_m^2\left(1-x^{\mathrm{v}}\right)}{d_{\mathrm{h}}\rho_{\mathrm{l}}}\right]\varphi_{\mathrm{l}}^2+G_m^2\frac{d}{dz}\left[\frac{\left(x^{\mathrm{v}}\right)^2}{\psi\rho_{\mathrm{v}}}+\frac{\left(1-x^{\mathrm{v}}\right)^2}{\left(1-\psi\right)\rho_{\mathrm{l}}}\right] \tag{3.28}$$

In Equation 3.28, d_h is the hydraulic diameter of the channel, and f, G_m, x^{v}, ρ, and ψ are the liquid-phase fanning friction factor, mass flux, vapor quality, density, and void fraction, respectively. z is the axial direction coordinate along the channel length. The Subscripts "l" and "v" represent liquid and vapor phase, respectively. In the two-phase multiplier correlation of Lockhart and Martinell[40], φ_l is incorporated with the A value proposed by Lee and Mudawar[41], Equations 3.29 to 3.31.

$$\varphi_{\mathrm{l}}^2=1+\frac{A}{X}+\frac{1}{X^2} \tag{3.29}$$

$$A=2.16\,\mathrm{Re}_{\mathrm{lo}}^{0.047}\,\mathrm{We}_{\mathrm{lo}}^{0.6}\ \text{(laminar liquid-laminar vapor)} \tag{3.30}$$

$$A=1.45\,\mathrm{Re}_{\mathrm{lo}}^{0.25}\,\mathrm{We}_{\mathrm{lo}}^{0.23}\ \text{(laminar liquid-turbulent vapor)} \tag{3.31}$$

Re_{lo} and We_{lo} are liquid-only Reynolds and Weber numbers, respectively. The Martinelli parameter, X, and the single phase empirical correlation of fanning friction factor for laminar flow in a rectangular channel by Shah and London[42] are expressed by Equation 3.32.

$$X=\left(\frac{\mu_{\mathrm{l}}}{\mu_{\mathrm{v}}}\right)^{0.5}\left(\frac{1-x^{\mathrm{v}}}{x^{\mathrm{v}}}\right)^{0.5}\left(\frac{\rho_{\mathrm{v}}}{\rho_{\mathrm{l}}}\right)^{0.5} \tag{3.32}$$

$$f\,\mathrm{Re}=24(1-1.3553\delta+1.9467\delta^2-1.7012\delta^3+0.9564\delta^4-0.2537\delta^5) \tag{3.33}$$

In Equation 3.32, μ is the viscosity and δ is the aspect ratio of the channel. Also, the void fraction model of Zivi[43] is adopted in this study.

The microchannel structures for the absorber and the desorber are adopted as a baseline, due to their ability to yield high heat and mass transfer rates and to minimize transport limitations on the performance; yet, the extent of potentially negative effect of the high viscosity of ILs on the pressure drop in microchannel heat/mass exchangers and, in turn, the system performance is critically assessed. The dimensions (length × width) of the evaporator and condenser are 2×2 cm, and 3×3 cm, respectively. The dimensions of the absorber and the desorber are 8×8 cm. The microfluidic channel cross-sectional area for the heat exchangers is 1×1 mm. The sizing of the heat exchangers is consistent throughout this thesis work including both theoretical and experimental analyses.

CHAPTER 4

ANALYSIS OF VARIOUS IL/REFRIGERANT WORKING FLUIDS USING THE NRTL MODEL

4.1 Introduction

In Chapter 4, the thermodynamic performance of a miniature absorption system using refrigerant/IL mixtures as the working fluid pairs was investigated. Small scale systems are of interest as possible cooling solutions for microprocessors and portable devices. Various mixtures of refrigerants and imidazolium ILs were compared among each other in terms of system efficiency and usability of the low-grade waste heat as the heat source of the system. The class of imidazolium ILs has been widely used in a variety of applications due to their attractive physical and chemical properties, like air and moisture stability, low flammability, thermal stability, being in the liquid state over a wide range of temperature, wide electrochemical windows, and high conductivities[44].

The ILs used in the present study include [emim][Tf_2N], [emim][BF_4], [bmim][BF_4], [bmim][PF_6], [hmim][Tf_2N], [hmim][BF_4], and [hmim][PF_6]; chemical names and structures are shown in Figure 4.1. Several HFC refrigerants, R125 (pentafluoroethane), R134a (1,1,1,2-tetrafluoroethane), R143a (1,1,1-trifluoroethane), R152a (1,1-difluoroethane), and R32 (difluoromethane), were investigated as the working fluid in the IL-based refrigeration system. Relevant characteristics of refrigerants, including ozone depletion potentials (ODP) and global warming potentials (GWP) are given in Table 4.1. The performance of an IL with R114 (dichlorotetrafluoroethane) and R124 (chlorotetrafluoroethane) were evaluated and compared to hydrofluorocarbon

refrigerants. Water, which is attractive due to its high thermal conductivity and latent heat of evaporation, was also explored as a refrigerant with IL absorbents. The structures of the Freon refrigerants explored in this work are shown in Figure 4.2.

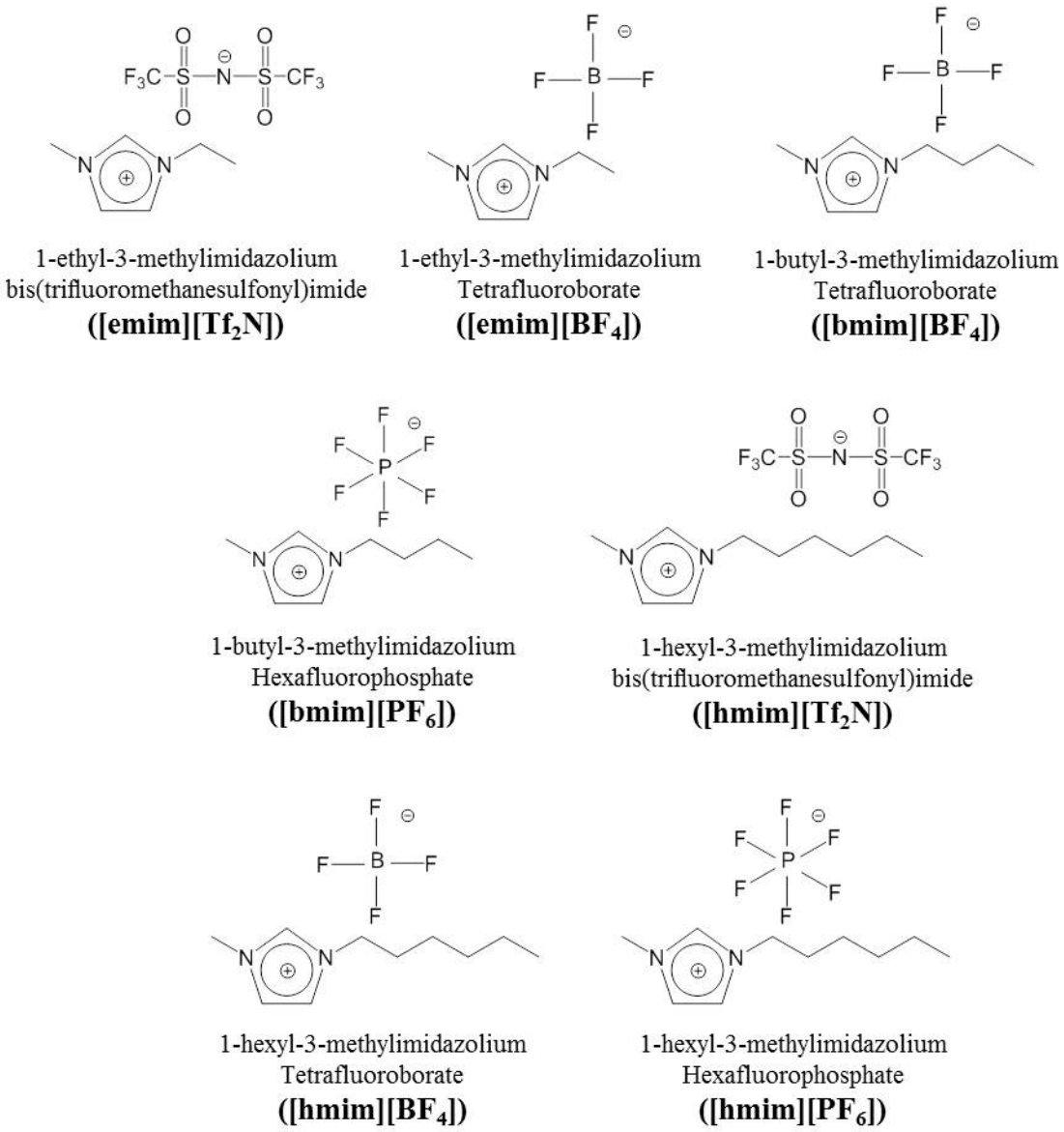

Figure 4.1: IL absorbent structures and names.

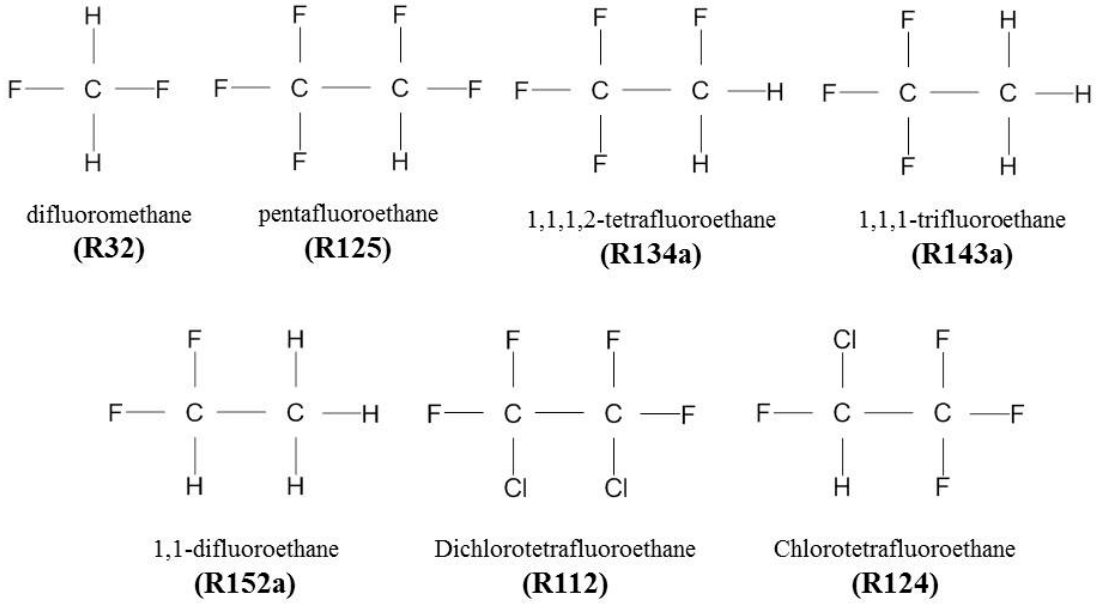

Figure 4.2: Refrigerant structures and names.

Table 4.1: Saturation pressures and latent heats of various refrigerants at the evaporator and condenser temperatures (T_e = 25°C, T_c = 50°C) and their ozone depletion potentials and global warming potentials[45].

Refrigerants	P_e^s **[kPa]**	P_c^s **[kPa]**	$\Delta h_{lv,e}$ **[kJ/kg]**	$\Delta h_{lv,c}$ **[kJ/kg]**	**ODP**[*]	**GWP**[**]
R114	214.4	446.9	128.07	117.53	1	3.9
R124	382.7	775.8	146.56	130.56	0.02	620
R125	1376.7	2533.2	110.4	76.4	0	3400
R134a	665.3	1317.9	177.8	151.8	0	1300
R143a	1262.3	2307.9	159.6	118.9	0	4300
R152a	596.4	1177.4	279.4	245.4	0	120
R32	1689.6	3141.2	270.9	209.6	0	620
Water	3.170	12.35	2441.7	2382.0	0	-

[*]The ODP of all other refrigerants are compared to R11[45]

[**]GWP is a relative scale which compares the greenhouse gas to carbon dioxide where GWP by definition is 1[45]

Since the feasibility and the compatibility of ILs as an absorbent of an absorption system in combination with refrigerants are the principal foci in this study, the performance of the system with respect to the refrigerant/IL mixtures is thermodynamically evaluated as a function of operating conditions. The effect of heat and mass transfer characteristics as well as the heat/mass exchangers' geometry would have an additional influence on the system performance, but is outside the scope of this primarily system level analysis[46].

The predicted mole fractions of the refrigerants in the IL mixture using the NRTL model are compared with the measured mole fraction data in the references[32,47–50] in Figure 4.3, which shows the good agreement between the measured and predicted data. The adjustable parameters used in the NRTL model are summarized in Table 4.2. The correlations based on group contribution methods were used to evaluate the viscosity[51], specific heat[52] and density[53] of the ILs. The solution heat exchanger is assumed to be ideal, i.e., to follow an isobaric process and with 100% heat exchanger efficiency.

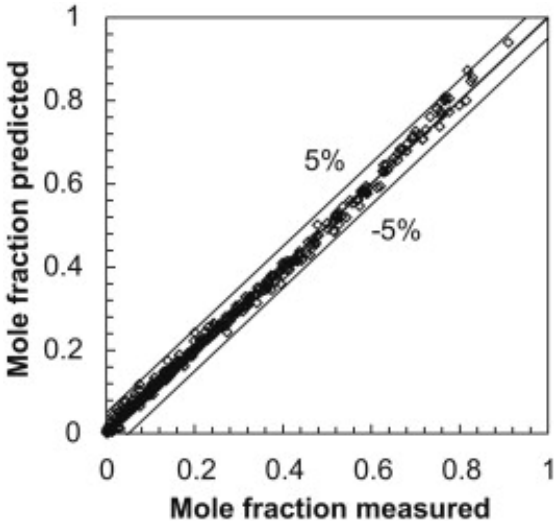

Figure 4.3: Comparison between the measured[32,47–50] and the predicted mole fractions of the refrigerants in the IL mixture using the NRTL model.

In all calculations, the operating temperature of the condenser and evaporator was set at 50^{o}C and 25^{o}C, respectively. The absorption temperature in subsections 4.2.1 and 4.2.2 is 35℃ .The cooling capacity of the evaporator was chosen to be 100 W. The outlet temperatures of the desorber and absorber were treated as adjustable parameters, which can be tuned to find the optimum operating conditions where the system efficiency reached its maximum value. The system performance in this thesis was analyzed at desorber temperatures between 65℃ and 100℃ in increments of 5℃ with connecting lines to clearly show the trend of the computed data points.

Table 4.2: Adjustable parameters in Equation 3.7.

Working fluid pair (1)/(2)	τ_{12}^{0} [-]	τ_{12}^{1} [K]	τ_{21}^{0} [-]	τ_{21}^{1} [K]
R134a/[emim][Tf_2N][47]	6.6710	-716.04	-0.8502	-262.85
R134a/[bmim][PF_6] [32]	1.2510	411.45	0.57596	-406.43
R134a/[hmim][Tf_2N] [47]	13.186	-2904.5	-5.3330	1128.9
R134a/[hmim][BF_4] [47]	7.5975	-1176.7	-0.26344	-275.97
R134a/[hmim][PF_6] [47]	11.718	-2397.7	-3.5270	688.02
R32/[bmim][BF_4] [32]	0.93194	553.36	0.36807	-585.91
R32/[bmim][PF_6] [32]	6.1356	-1194.6	-1.9069	122.26
R125/[bmim][PF_6] [32]	2.4582	48.172	1.6394	-563.00
R143a/[bmim][PF_6] [32]	5.2848	-18.277	-0.11097	-68.435
R152a/[bmim][PF_6] [32]	6.5351	-871.79	-0.02731	-409.50
R114/[emim][Tf_2N] [48]	2.0631	1549.9	-1.0567	390.84
R124/[emim][Tf_2N] [48]	0.11312	1210.1	1.4565	-1040.3
Water/[emim][Tf_2N][49]	1.7388	1074.7	-4.9829	1369.1
Water/[emim][BF_4][50]	17.253	-6445.4	-12.650	4426.8

4.2 Results and Discussion

4.2.1 Effect of the Desorber Outlet Temperature

Figure 4.4 shows the CE variation of the absorption system with respect to desorber outlet temperature for several working fluid pairs. Figure 4.4 shows a relatively sharp rise in CE up to ~80^{o}C followed by a more constant value as the desorber outlet temperature rises beyond 80^{o}C. The variation of the desorber outlet temperature affects the concentration of refrigerant in the strong solution, which can be approximated by Equation 4.1.

$$x_{\mathrm{s}} \approx \frac{P_{\mathrm{c}}}{\gamma_s P^s\left(T_8\right)} \tag{4.1}$$

P_{c} is the vapor pressure at the condenser and $P^s\left(T_8\right)$ is the saturation vapor pressure at T_8. Superscript s represents the saturation. As the temperature increases, the refrigerant mole fraction decreases. The flow rate of the solution will then vary correspondingly. The circulation ratio, α, is the amount of solution flow rate of the refrigerant/IL mixture needed to achieve compression for a given mass flow rate of the refrigerant, as given by Equation 4.2.

$$\alpha \equiv \frac{\dot{m}_w}{\dot{m}_r} = \frac{\left(1-x_{\mathrm{s}}^m\right)}{\left(x_w^m - x_{\mathrm{s}}^m\right)} \tag{4.2}$$

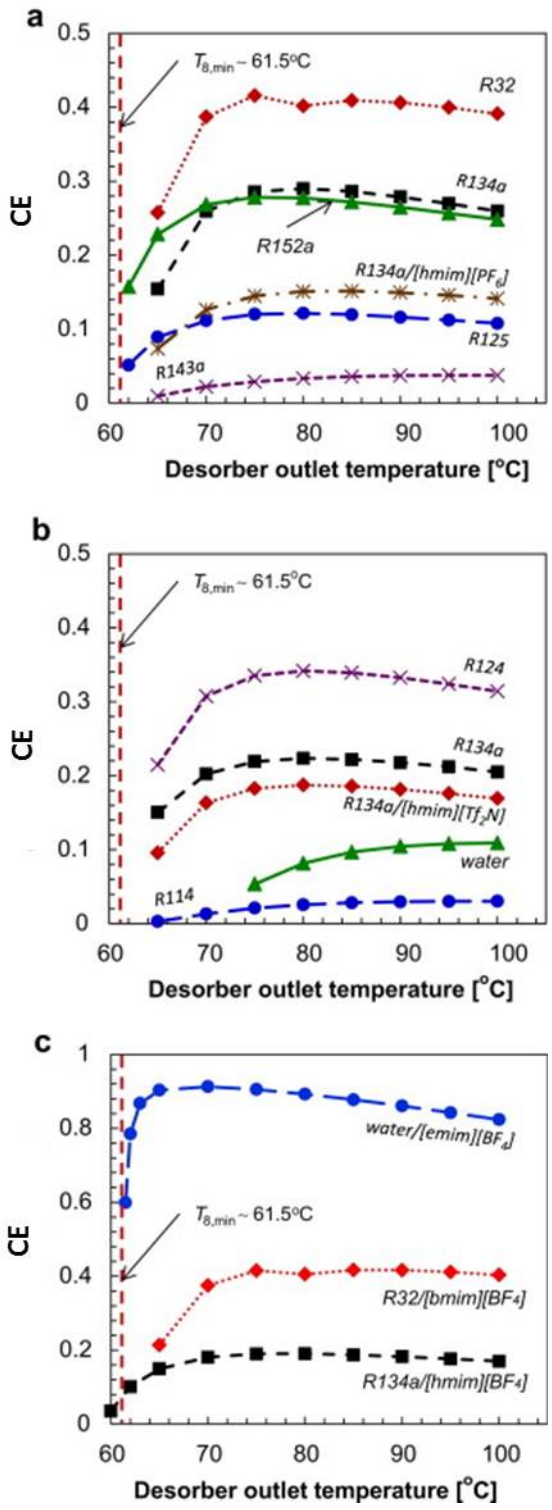

Figure 4.4: CEs of the absorption system with respect to the desorber outlet temperature using different working fluid pairs:(a) refrigerant/[bmim][PF_6] and R134a/[hmim][PF_6]; (b) refrigerant/[emim][Tf_2N] and R134a/[hmim][Tf_2N]; (c) R134a/[hmim][BF_4], R32/[bmim][BF_4] and water/[emim][BF_4].

The circulation ratio increases with mass fraction in the strong solution, at fixed refrigerant mass fraction in the weak solution. Figure 4.5 shows the circulation ratio variation with respect to the desorber outlet temperature. The increase in desorber outlet temperature reduces the circulation ratio due to a decrease in the mass fraction of the strong solution. Equation 2.9 can be rewritten to yield Equation 4.3.

$$\frac{Q_d}{m_r} = \alpha\left(h_8 - h_7\right) - h_8 + h_3 \tag{4.3a}$$

$$\frac{Q_d}{m_r} = h_8\left(\alpha - 1\right) + h_3 - \alpha h_7 \tag{4.3b}$$

Equation 4.3a shows that a smaller circulation ratio results in less heat input to the desorber for the same amount of cooling at the evaporator, which would increase CE. Thus, a lower circulation ratio resulting from the temperature increase (Figure 4.5) increases CE at low desorber outlet temperatures (<80^{o}C), as shown in Figure 4.4. However, as the temperature further increases, the change rate of the circulation ratio ($\partial\alpha/\partial T_8$) is diminished (Figure 4.5). Also, the increase in enthalpies of the desorber outlet (h_3 and h_8) accompanied by the increase of the temperature require larger heat input to the desorber, Equation 4.3b. Consequently, at high desorber outlet temperatures, the effect of the reduced circulation ratio and the increased enthalpy on the heat input to the desorber conflicts and the effect on CE cancels each other out. This leads to a leveling off of the CEs in Figure 4.4.

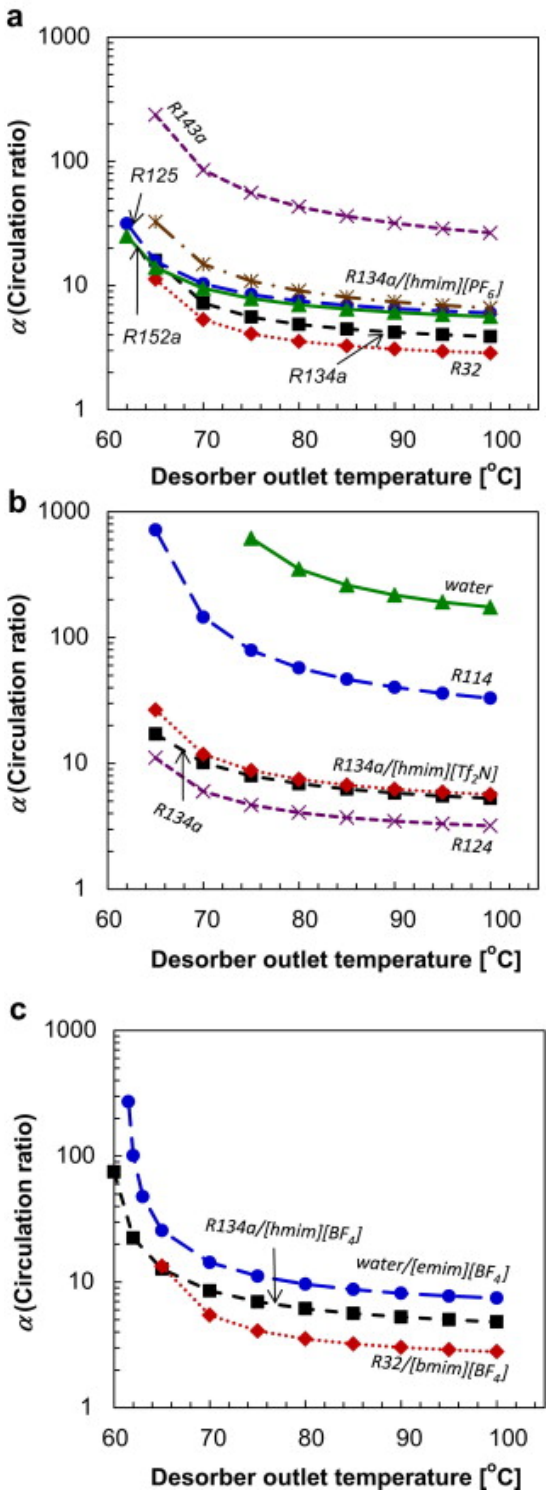

Figure 4.5: Circulation ratios of the absorption system with respect to the desorber outlet temperature using different working fluid pairs: (a) refrigerant/[bmim][PF_6] and R134a/[hmim][PF_6]; (b) refrigerant/[emim][Tf_2N] and R134a/[hmim][Tf_2N]; (c) R134a/[hmim][BF_4], R32/[bmim][BF_4] and water/[emim][BF_4].

The refrigerant mole fraction for the weak solution is approximated in Equation 4.4.

$$x_w \approx \frac{P_e}{\gamma_w P^s(T_5)} \tag{4.4}$$

Assuming $\gamma_s \approx \gamma_w$, Equations 4.1 and 4.4 can be written to yield Equations 4.5 and 4.6 using the inequality, $x_w > x_s$.

$$P^s(T_8) > \frac{P_c}{P_e} P^s(T_5) \tag{4.5}$$

$$T_8 > T^s\left(\frac{P_c}{P_e} P^s(T_5)\right) \approx T_{8,\min} \tag{4.6}$$

From Equation 4.6, it can be seen that the lower bound on the desorber outlet temperature, or maximum operating temperature of the system, is a function of the operating conditions, i.e., vapor pressures at the evaporator and condenser as well as the absorber outlet temperature. Figure 4.4 also shows that the CE curves generally converge to zero at T_8 ~ 61.5^{o}C (dashed line) for all refrigerants. Thus, the CE curves can be shifted to lower temperature by adjusting the operating conditions so as to have optimum performance at a lower temperature, ca. 60^{o}C. Then, the utilization of waste-heat can be optimized.

4.2.2 Effect of Refrigerant/IL Compatibility

The R32/[bmim][PF_6] pair showed the highest CE ~0.42, of all the refrigerant pairs in Figure 4.4(a). The CE values for R134a and R152a with [bmim][PF_6] were moderate, while for R125 and R143a were lower. Note that the CE trends for the HFC

refrigerants in Figure 4.4(a) approximately correlate with the refrigerant mass fraction in the weak solution, x_w^m, listed in Table 4.3.

Table 4.3: Refrigerant mass fractions in the weak solution.

Working fluid pair (1)/(2)	x_w^m
R143a/[bmim][PF_6]	0.0787
R125/[bmim][PF_6]	0.2210
R134a/[hmim][PF_6]	0.2563
R152a/[bmim][PF_6]	0.2286
R134a/[bmim][PF_6]	0.3239
R32/[bmim][PF_6]	0.4362
R114/[emim][Tf_2N]	0.0599
Water/[emim][Tf_2N]	0.0091
R134a/[hmim][Tf_2N]	0.2910
R134a/[emim][Tf_2N]	0.2676
R124/[emim][Tf_2N]	0.3972
R134a/[hmim][BF_4]	0.2791
R32/[bmim][BF_4]	0.4487
Water/[emim][BF_4]	0.1542
Water/[emim][Tf_2N]	0.0091

Equation 4.7 shows the relation between the mass fraction and mole fraction.

$$x^m = \frac{xM_r}{xM_r + (1-x)M_{IL}} \tag{4.7}$$

M_r and M_{IL} are the molecular weights of refrigerant and IL, respectively. The effect of the weak solution solubility on the performance is attributed to the smaller circulation ratio brought about by a larger value of refrigerant mass fraction in the weak solution. Thus, it can be stated that the high solubility of refrigerant (mass fraction solubility) in the IL solution improves the performance of the absorption system. However, the higher solubility of R134a in [hmim][Tf_2N] results in a lower CE value relative to R134a/[emim][Tf_2N] in Figure 4.4(b). Ren and Scurto[47] compared the solubility (mole fraction solubility) of R134a in [emim][Tf_2N] and R134a in [hmim][Tf_2N]. They reported that a longer alkyl chain length on the cation (i.e. $hmim^+$ vs. $emim^+$) increased the solubility of R134a. Shiflett et al.[32] and Aki et al.[54] measured the solubility of R32 and carbon dioxide in the ILs, respectively. They both found that the solubility of the gas in the IL can be increased by increasing the alkyl chain length on the organic cation, which is in agreement with the results in Figure 4.6(b). On the other hand, Kerle et al.[55] investigated the temperature dependence of the solubility of carbon dioxide in imidazolium-based ILs and showed that as the alkyl chain length increases, the solubility becomes less sensitive to temperature. The temperature coefficient of solubility is directly related to the entropy of mixing in Equation 4.8[56–59].

$$\left(\frac{\partial \ln x_2}{\partial \ln T}\right)_P = \frac{\Delta \bar{s}_r}{R\left(\partial \ln a_2 / \partial \ln x_2\right)_{P,T}} \tag{4.8}$$

$\Delta\overline{s}_r$ is the entropy of mixing (or relative partial molar entropy) of the refrigerant in the solution, and a_2 is the activity of the refrigerant in the solution, as given by Equation 4.9.

$$a_2 = \gamma_2 x_2 \tag{4.9}$$

In the Henry's law regime (i.e., when γ_2 is independent of x_2), the derivative in the right-hand side dominator in Equation 4.8 becomes unity. Therefore, the equation can be reduced to the van't Hoff form[58] as shown in Equation 4.10.

$$\Delta\overline{s}_r = R\left(\frac{\partial \ln x_2}{\partial \ln T}\right)_P \tag{4.10}$$

Integrating Equation 4.10 yields[59] Equation 4.11.

$$\left(\ln x_2\right)_P = \frac{\Delta\overline{s}_r}{R}\ln T + D \tag{4.11}$$

In Equation 4.11, *D* is an integration constant. Since the relative partial molar entropy is reduced by increasing the alkyl chain length, Equation 4.11 supports the reduced dependence of the refrigerant mass fraction on the desorber outlet temperature. In summary, longer cation alkyl chain length causes a higher solubility but lower dependence of the solubility on temperature. These effects of the cation result in a larger circulation ratio for R134a/[hmim][Tf_2N], as shown in Figure 4.5(b), because the refrigerant mass fraction difference between the weak and strong solutions in Equation 4.2, ($x_w^m - x_s^m$), is lower due to the reduced dependence of the solubility on temperature with the longer alkyl chain length of $[hmim]^+$. Thus, even with a larger refrigerant solubility in the weak solution, the performances of the system can be degraded due to the reduced dependence of the solubility on temperature. R143a/[bmim][PF_6] and R134a/[hmim][PF_6] are remarkably less sensitive to temperature (Figure 4.6(a)) and

show relatively low CEs (Figure 4.4(a)). Water solubility in [emim][Tf_2N] depends more on the desorber outlet temperature (Figure 4.6(b)), but refrigerant mass fraction in the weak solution is extremely low resulting in a large circulation ratio and thereby low CE, as shown in Figure 4.5(b) and Figure 4.4(b), respectively.

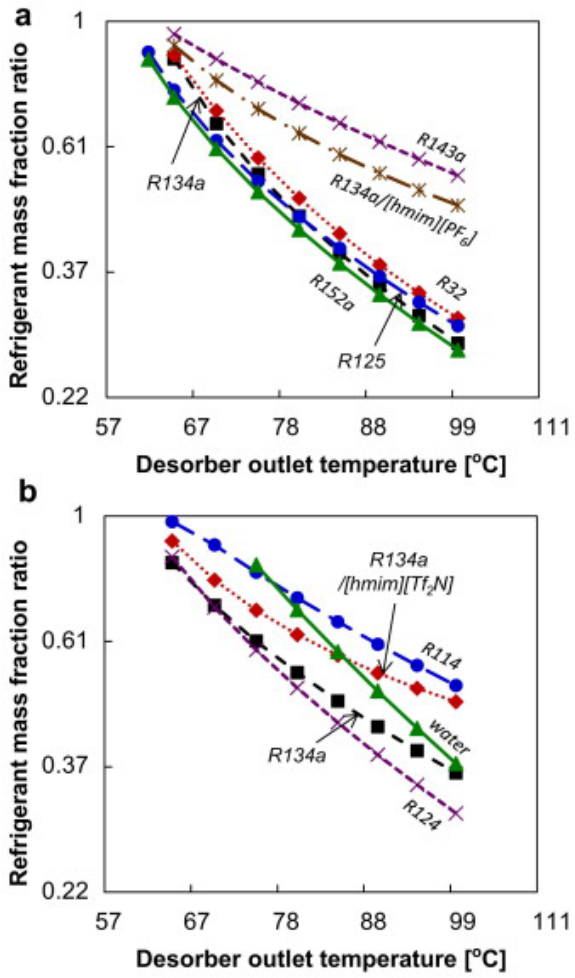

Figure 4.6: Refrigerant mass fraction ratio in the strong solution relative to the weak solution ($\ln x_s^m / x_w^m$) of the absorption system with respect to the desorber outlet temperature ($\ln T_8$) using different working fluid pairs: (a) refrigerant/[bmim][PF_6] and R134a/[hmim][PF_6]; (b) refrigerant/[emim][Tf_2N] and R134a/[hmim][Tf_2N]; (c) R134a/[hmim][BF_4], R32/[bmim][BF_4] and water/[emim][BF_4].

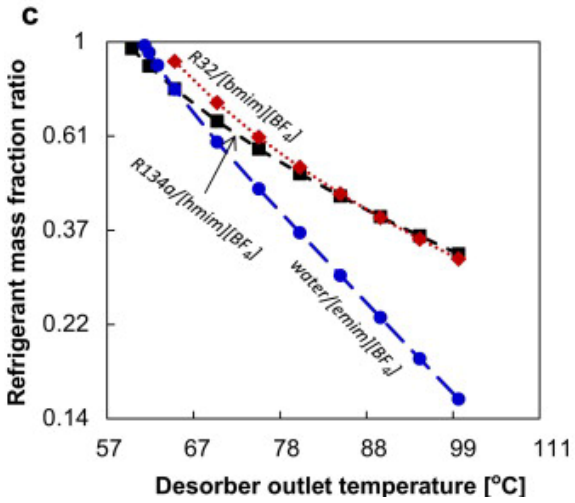

Figure 4.6 continued.

The CE values for the absorption system using the water/[emim][BF_4] pair are notably higher than those with the other working fluid pairs (Figure 4.4(c)). The maximum CE was 0.91 at T_d = 70°C. The imidazolium-$[BF_4]^-$ ILs have dramatically higher solubility for water (Figure 4.5(c)), while ILs with $[Tf_2N]^-$ show poor water solubility[25] as shown in Figure 4.5(b). The low CE values of water/[emim][Tf_2N] in Figure 4.4(b) are attributed to the low solubility of water in [emim][Tf_2N]. However, the refrigerant mass fraction of water in [emim][BF_4] is less than that of R32 in [bmim][BF_4] (Figure 4.6(c)). Moreover, the circulation ratio of water is the highest among the refrigerants for imidazolium-$[BF_4]^-$ in Figure 4.5(c), by which the lower CE is expected than that of R32 in [bmim][BF_4]. This suggests that there should be another factor affecting the performance of the absorption system, other than solubility and circulation ratio. The latent heat of vaporization for water is an order of magnitude higher than that of the other refrigerants, as listed in Table 4.1. Then, the required mass flow rate of water to produce the target 100 W cooling capacity at the evaporator is significantly smaller

(Table 4.4). It is evident from Equation 4.3 that the low water flow rate contributes to reducing the heat input required at the desorber, Q_d. Consequently, this leads to high CE values for the water/[emim][BF_4] pair shown in Figure 4.4(c). Similarly, the refrigerants R152a and R32 also have large latent heats and small refrigerant mass flow rates. This improves the system performance when using these working fluid pairs.

Table 4.4: Refrigerant mass flow rates in the absorption system.

Refrigerants	Refrigerant flow rate [g/s]
R114	0.897
R124	0.785
R125	1.155
R134a	0.651
R143a	0.761
R152a	0.402
R32	0.420
Water	0.042

4.2.3 Effect of IL Viscosity

Higher viscosity ILs cause an increase in the pressure drop in the compression loop, which would result in larger pumping power or larger pipes and system volume. Figure 4.7 shows the viscosity of pure ILs vs. temperature evaluated using the group

contribution method[51]. The viscosity increases with cation mass: $emim^+$<$bmim^+$<$hmim^+$. The viscosity is more dependent on the anion with the following order: Tf_2N^-<BF_4^-<PF_6^-. The viscosity of [emim][Tf_2N] is only 31.3 mPa·s at 294K, which is 10 times smaller than that of [hmim][PF_6].

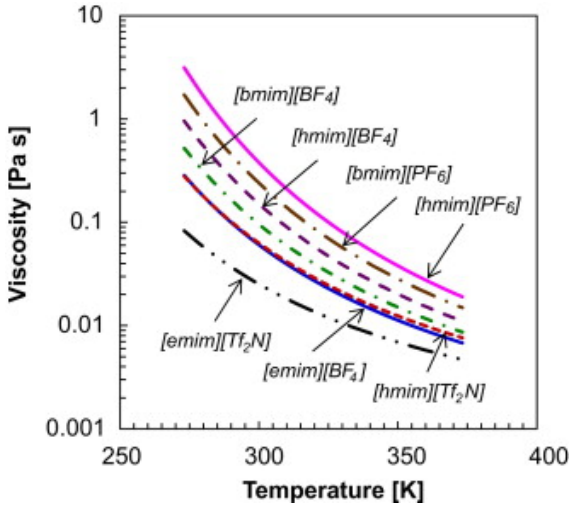

Figure 4.7: Viscosities of ILs evaluated using group contribution method[51].

Figure 4.8 shows the total pumping power of the absorption system for various refrigerants/IL pairs. It is very encouraging that for most of the working fluid pairs, except R125/[bmim][PF_6], R143a/[bmim][PF_6], and R114/[emim][Tf_2N], the pumping power was less than 10 W for the 100 W cooling capacity system. The total pumping power can be calculated using Equations 4.12 and 4.13.

$$W_p = \dot{m}_s \left(P_c - P_e + \Delta P_{drop} \right) \tag{4.12}$$

$$\frac{W_p}{\dot{m}_r} = \alpha \left(P_c - P_e + \Delta P_{drop} \right) \tag{4.13}$$

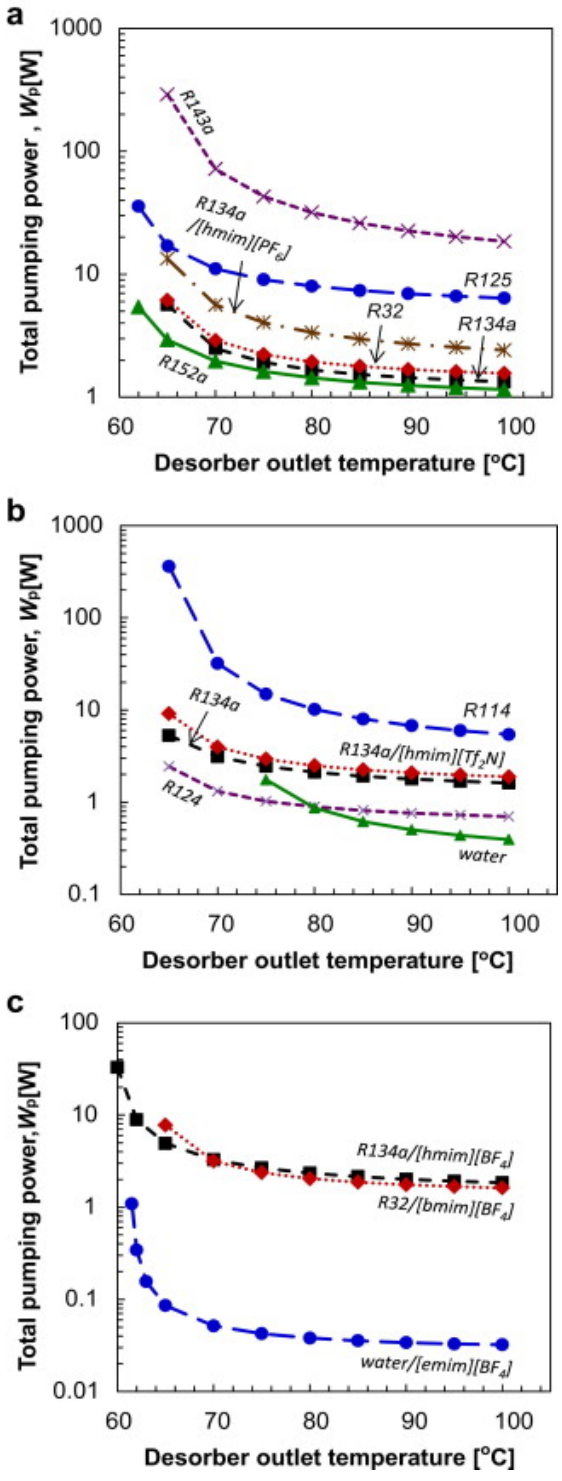

Figure 4.8: Total pumping power consumptions of the absorption system with respect to the desorber outlet temperature using different working fluid pairs: (a) refrigerant/[bmim][PF_6] and R134a/[hmim][PF_6]; (b) refrigerant/[emim][Tf_2N] and R134a/[hmim][Tf_2N]; (c) R134a/[hmim][BF_4], R32/[bmim][BF_4] and water/[emim][BF_4].

ΔP_{drop} is the pressure drop due to two phase pressure drop in microchannel based heat exchangers (Equation 3.28). The circulation ratio plays an important role in the pumping power, as well. Since a lower solution flow rate is accompanied by a reduction in the circulation ratio at higher desorber temperatures, as shown in Equation 4.13, lower pumping power values result from a higher desorber temperature. Also, COP (ratio of the evaporator cooling capacity to the pumping power) improves as the pumping power decreases at higher desorber temperatures, as shown in Figure 4.9. Due to the small flow rate of water, $\dot{m}_r$, the pumping power becomes negligible, resulting in very high COP values for the water/[emim][Tf_2N] pair. However, it should be noted that even though the COP values are large for water/[emim][Tf_2N], the low value of CE requires large desorber and absorber heat exchangers.

Figure 4.10 shows the ratio of pumping power due to pressure drop to the total pumping power. For most working fluid pairs, less than 10% of the total pumping power is attributed to pressure drop. The pressure drop attributes from the friction and acceleration of the fluid in the microchannels. Most of the pumping power is used to pressurize the refrigerant/IL pair, $\left(P_c - P_e\right)$, which is the reason that R32 shows the smallest pressure drop contribution while water has the largest. Since the pressure difference between the condenser and evaporator with water is only 9.2 kPa, which is negligibly small and less than 1% of the pressure difference of R32, more than 90% of the pumping power for the water/[emim][Tf_2N] and water/[emim][BF_4] was used to overcome the pressure drop. For the R143a/[bmim][PF_6] and R114/[emim][Tf_2N] pairs, the high solution flow rate, $\dot{m}_w$, resulted from high circulation ratios and, in turn, caused large values of pumping power due to pressure drop.

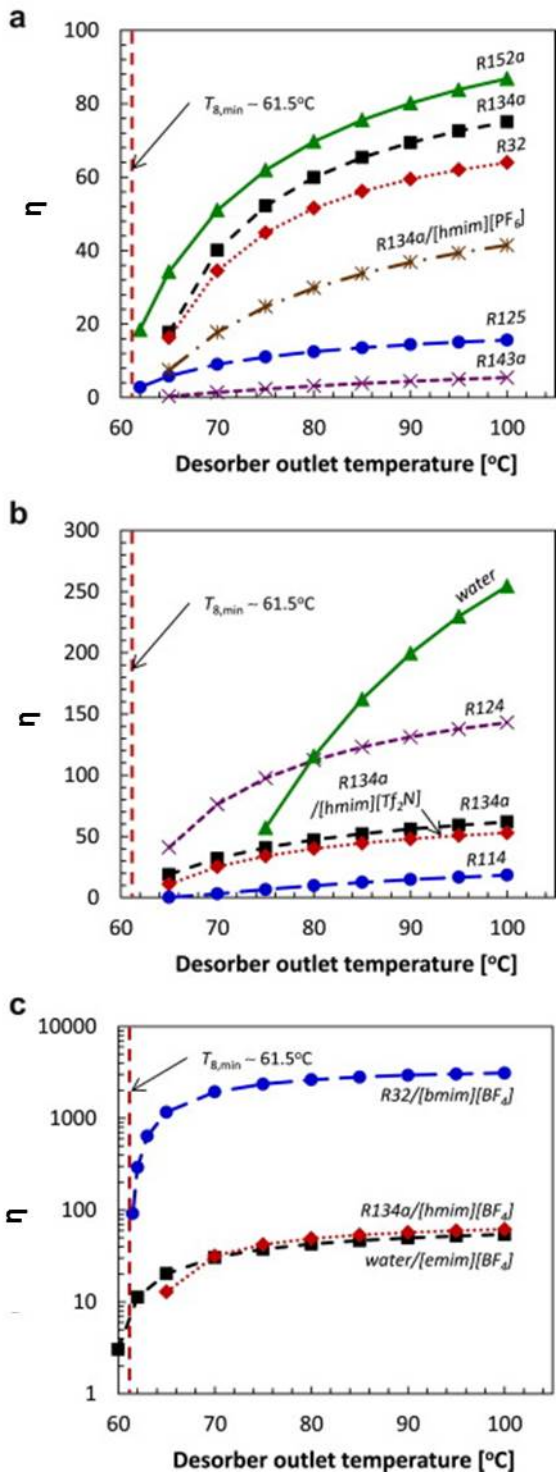

Figure 4.9: COP (η) of the absorption system with respect to the desorber outlet temperature using different working fluid pairs: (a) refrigerant/[bmim][PF_6] and R134a/[hmim][PF_6]; (b) refrigerant/[emim][Tf_2N] and R134a/[hmim][Tf_2N]; (c) R134a/[hmim][BF_4], R32/[bmim][BF_4] and water/[emim][BF_4].

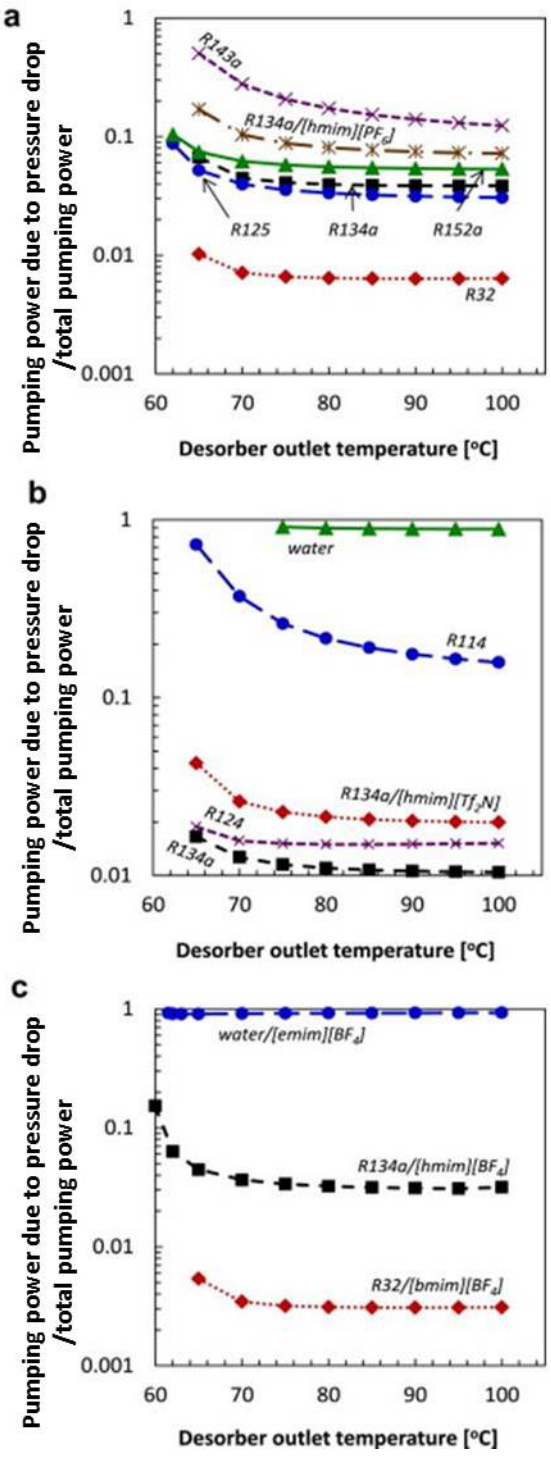

Figure 4.10: Pumping power consumptions of the absorption system caused by two phase pressure drop in heat exchangers with respect to the desorber outlet temperature using different working fluid pairs: (a) refrigerant/[bmim][PF_6] and R134a/[hmim][PF_6]; (b) refrigerant/[emim][Tf_2N] and R134a/[hmim][Tf_2N]; (c) R134a/[hmim][BF_4], R32/[bmim][BF_4] and water/[emim][BF_4].

The relatively small contribution of friction to the total pumping power was mainly because of the low viscosity of the mixtures due to dilution contributed by the refrigerants. However, it also should be noted that the heat exchanger microchannel cross-sectional area was slightly larger than that of conventional microfluidic channels. As shown in Equation 3.33, the laminar flow friction factor is inversely proportional to the Reynolds number, $f_l \sim Re^{-1} \sim \mu / G d_h$. Under fixed mass flow rate, mass flux is inversely proportional to the channel cross-sectional area, $G \sim A_{cs}^{-1} \sim 4/\pi d_h^2$, where A_{cs} is the channel cross-sectional area. Assuming that the two-phase multiplier, $\varphi_l^2 = \left(dP/dz\right)_{TP} / \left(dP/dz\right)_l$, is a weak function of diameter, Equation 3.28 shows that the frictional pressure drop, which is the first bracket of the right-hand side of the equation, can be given by Equation 4.14.

$$\left(\frac{dP}{dz}\right)_{friction} = \left[\frac{2 f_l G^2 \left(1 - x^{\mathrm{v}}\right)}{d_{\mathrm{h}} \rho_{\mathrm{l}}}\right] \varphi_{\mathrm{l}}^2 \sim \frac{G}{d_h^2} \sim d_h^{-4} \tag{4.14}$$

Thus, small adjustments in the microfluidic channel dimensions can have a large effect on the pumping power for systems with high viscosity.

4.2.4 Effect of the Absorber Outlet Temperature

The absorber outlet temperature is controlled by the ambient cooling temperature. A lower absorber temperature enhances the CE of the system, as shown in Figure 4.11. As the absorber outlet temperature rises, the solubility of the weak solution decreases, as determined by Equation 4.4. Thus, the difference in mole fraction between the strong and weak solutions is diminished, which leads to a larger circulation ratio and lower CE. The increase in the desorber inlet enthalpy, h_7, driven by the absorber outlet temperature

increase, also contributes to the enhancement of CE by reducing the required heat input to the desorber, Q_d. However, the effect of the circulation ratio change on CE dominates, so that the monotonic decrease in CE, with respect to the absorber temperature increase, is observed in Figure 4.11.

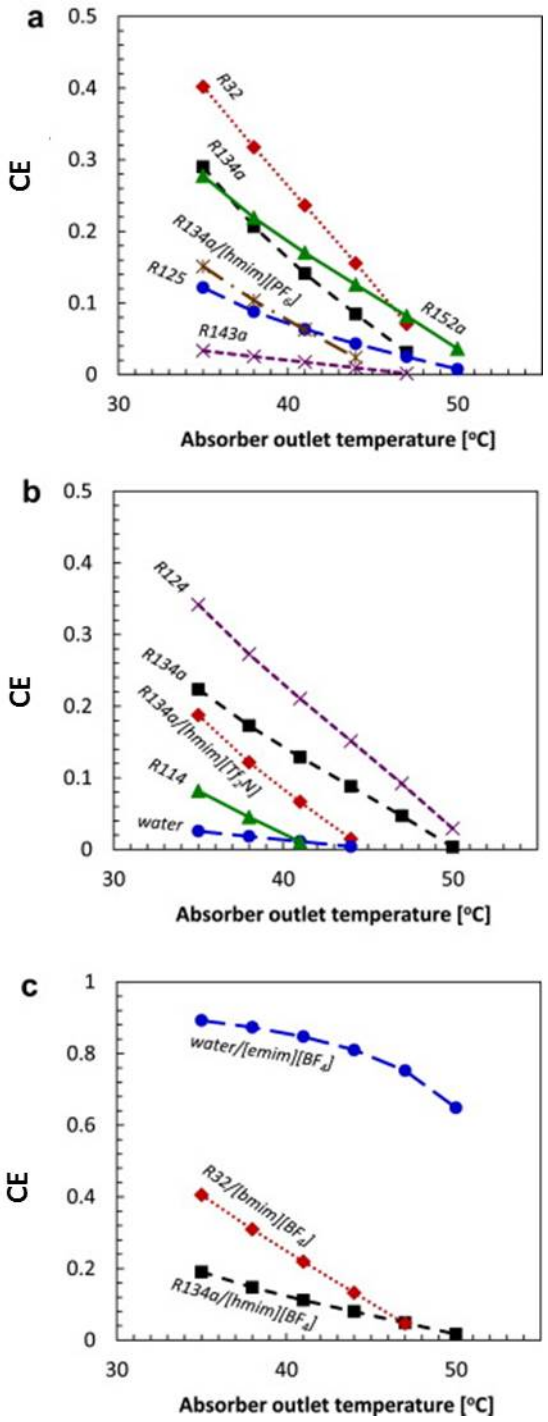

Figure 4.11: CEs of the absorption system with respect to the absorber outlet temperature using different working fluid pairs: (a) refrigerant/[bmim][PF_6] and R134a/[hmim][PF_6]; (b) refrigerant/[emim][Tf_2N] and R134a/[hmim][Tf_2N]; (c) R134a/[hmim][BF_4], R32/[bmim][BF_4] and water/[emim][BF_4].

4.3 Conclusion

The feasibility of several refrigerant/IL mixtures as working fluid pairs for the absorption based refrigeration system was numerically evaluated. The refrigerant/IL compatibility indicated by the circulation ratio was one of the most important factors in determining the system performance with the new working fluid pairs. The solubility of the refrigerants in the ILs and their temperature dependence affected the circulation ratio. R32 showed the lowest circulation ratio with relatively high CE values for the ILs having $[PF_6]^-$ and $[BF_4]^-$ anions. Although R124 showed the best compatibility and performance with $[Tf_2N]^-$, due to its negative environmental impact, R124 may not be the optimum choice of refrigerant. Cations with shorter alkyl chains are preferred ($[emim]^+ > [bmim]^+ > [hmim]^+$) due to more sensitive dependence of the solubility on temperature. Overall, water/[emim][BF_4] showed the highest CE value, ca. 0.91, where the improved compatibility of water with [emim][BF_4] and the superior properties of water as a heat transfer fluid, such as large latent heat of evaporation, followed by extremely small refrigerant (water) flow rate resulted in its high performance. Using water with [emim][Tf_2N] has not been found promising due to the extremely low solubility of IL in water (Table 4.3). Lafrate et al.[60], however, showed that diol-functionalized ILs with $[Tf_2N^-]$ can be completely water-miscible, which could potentially deliver an improved performance of the absorption system. However, the evaporator and condenser temperature and pressure values for water (as the refrigerant) are not of interest for most electronic cooling applications. The effect of the higher viscosity of the ILs on the pressure drop and pumping power were mitigated by slightly increasing the microfluidic channel cross-sectional area. The absorber outlet temperature significantly affected the

system performance. Lowering the absorber outlet temperature is desirable due to the increased solubility of the refrigerant in the IL. The system level numerical investigation showed that refrigerant/IL pairs are promising materials for absorption refrigeration utilizing low-grade waste heat, as found in electronic systems.

CHAPTER 5

ANALYSIS OF HYDROFLUOROCARBON/[bmim][PF_6] WORKING FLUIDS USING THE EOS MODEL

5.1 Introduction

The non-random two-liquid (NRTL) model has been commonly used to fit the experimental solubility of refrigerants in absorbents because of its simplicity and good approximation of solubility values[32,61]. However, it is preferable to use a model that can be used to calculate pure component and mixture properties in multi-phase systems in addition to having good accuracy over a wide range of temperatures and pressures. Solution models (including the NRTL model) are limited in their usefulness at temperatures below the refrigerant critical temperature, and the combined use of empirical-fitting equations with the gas phase equation-of-state (EOS) may not always be consistent at high generator-temperatures[34]. In the case of pentafluoroethane (R125), the critical temperature is 351.56K[29], which will limit the desorber temperature of the system. Thus, the Redlich-Kwong type EOS was employed for improved modeling of the system. The EOS model allows computation of precise mixture properties, compositions, and state conditions such as mixture enthalpy, vapor quality, and fluid temperature. A two-phase pressure drop equation (Equation 3.28) was introduced into the EOS model to evaluate the friction loss due to pumping the viscous IL, which will affect the pumping work and system efficiency. In this study, [bmim][PF_6] was used as the IL and five different hydrofluorocarbon (HFC) refrigerants (R134a, R32, R125, R143a, R152a) were analyzed. [bmim][PF_6] was selected as the absorbent because of its high molar uptake of

freons, which is essential to deliver maximum cooling. The effect of a counter-flowing solution heat exchanger, desorber temperature, and absorber temperature on the system performance was investigated. For the calculations, two values of heat exchanger efficiency, 25% and 40% ($\varphi = 0.25$ or 0.40), were used and compared.

5.2 Results and Discussion

5.2.1 System Parameters

The solubility data for HFC and [bmim][PF_6] mixtures are taken from Shiflett and Yokozeki[32]. The critical properties along with EOS constants and ideal gas heat capacities of the compounds used in this work are shown in Tables 5.1 and 5.2, respectively.

Table 5.1: Critical properties and EOS constants of [bmim][PF_6] and HFC refrigerants.

Pure compound	T_c **(K)**	P_c **(kPa)**	β_0	β_1	β_2	β_3
[bmim][PF_6][62]	860.5	2645	1.0	0.62627	0	0
R32[34]	351.26	5782	1.0019	0.48333	-0.07538	0.00673
R125[34]	339.19	3637	1.0001	0.47736	-0.01977	-0.0177
R134a[34]	374.21	4059	1.0025	0.50532	-0.04983	0
R143a[34]	346.20	3759	1.0006	0.45874	-0.04846	-0.0143
R152a[34]	386.44	4520	1.0012	0.48495	-0.08508	0.0146

The BIPs for refrigerants/IL pairs were found and used to compute solubility values at different temperature and pressure conditions. The optimum BIPs found for

different working fluids are summarized in Table 5.2. Figures 5.1 show the solubility of five HFCs in [bmim][PF_6], where the different lines are isotherms modeled by the EOS, and the symbols indicate experimental data at the same temperatures used to develop the EOS correlations. It can be seen that the quality of the RK correlation is adequate for an entire range of experimental parameters to be useful for the system performance calculations.

Table 5.2: Coefficients for ideal gas heat capacity of pure compounds [$J \cdot mol^{-1}$].

Pure compound	C_p^0 **(J·mol^{-1})**	C_p^1 **(J·mol^{-1}K^{-1})**	C_p^2 **(J·mol^{-1}K^{-2})**	C_p^3 **(J·mol^{-1}K^{-3})**
[bmim][PF_6][7]	-2.214	0.57685	-3.854×10^{-4}	9.785×10^{-8}
R32[34]	20.34	0.07534	1.872×10^{-5}	-3.116×10^{-8}
R125[34]	16.58	0.33983	-2.873×10^{-4}	8.870×10^{-8}
R134a[34]	12.89	0.30500	-2.342×10^{-4}	6.852×10^{-8}
R143a[34]	5.740	0.31388	-2.595×10^{-4}	8.410×10^{-8}
R152a[34]	8.670	0.2394	-1.456×10^{-4}	3.392×10^{-8}

Table 5.3: Binary interaction parameters for [bmim][PF_6] and HFC refrigerants.

Fluid pair	$l_{12} = l_{21}$	k_{12}	τ_{12} **(K)**	ΔP**(MPa)**[a]
R32/[bmim][PF_6]	0.0295	-0.0167	13.9407	0.010
R125/[bmim][PF_6]	0.1865	-0.2545	78.5937	0.009
R134a/[bmim][PF_6]	0.1278	-0.1504	41.9269	0.005
R143a/[bmim][PF_6]	-0.239	0.1948	50.1348	0.004
R152a/[bmim][PF_6]	-0.2496	0.2112	70.1631	0.006

[a]Standard deviations of non-linear least squares in pressures.

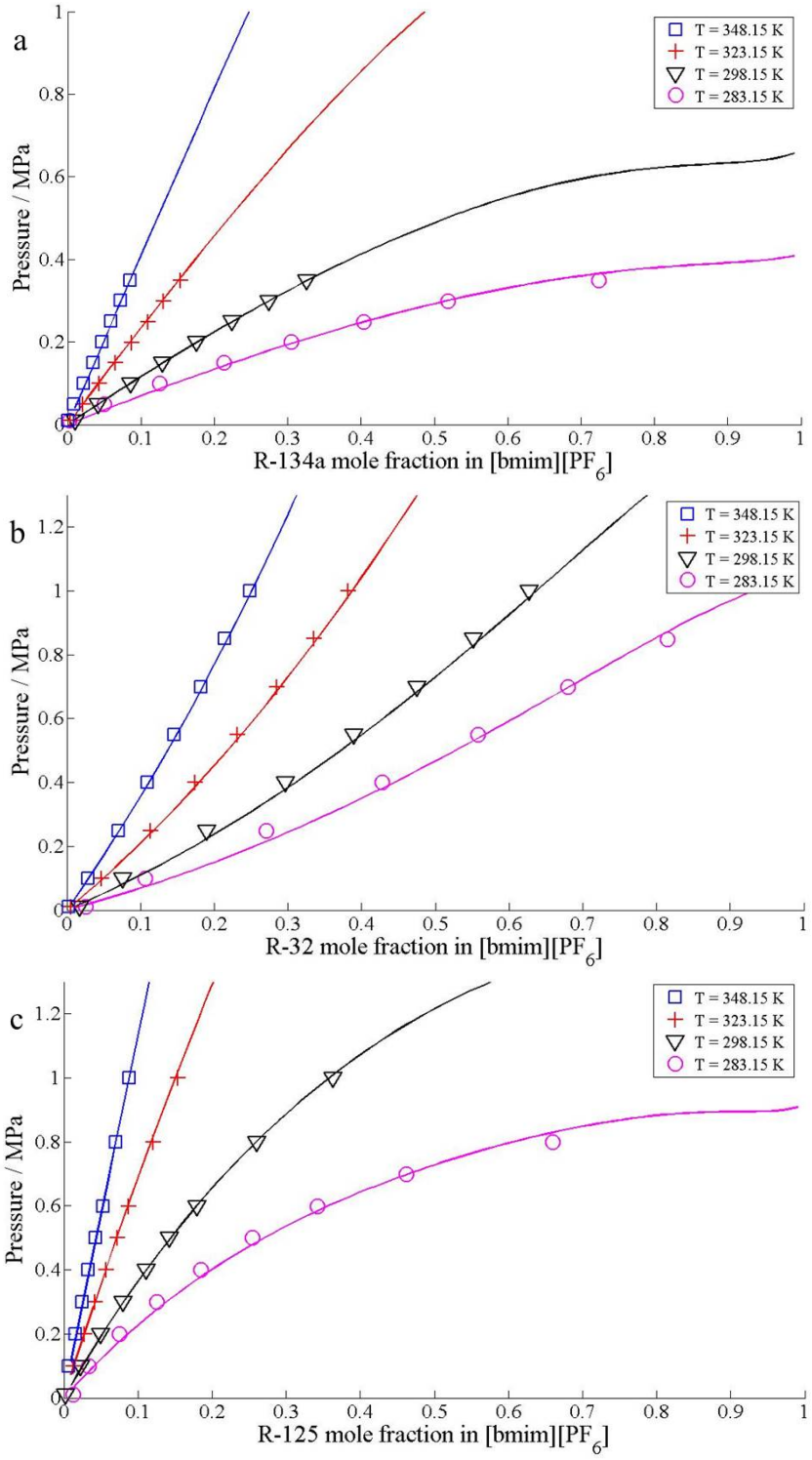

Figure 5.1: Solubility of HFC refrigerants in [bmim][PF_6] as a function of temperature [K] and pressure [MPa]; (a) R134a; (b) R32; (c) R125; (d)R143a; (e)R152a. Symbols: experimental solubility data[32]; lines: computed EOS model using BIPs.

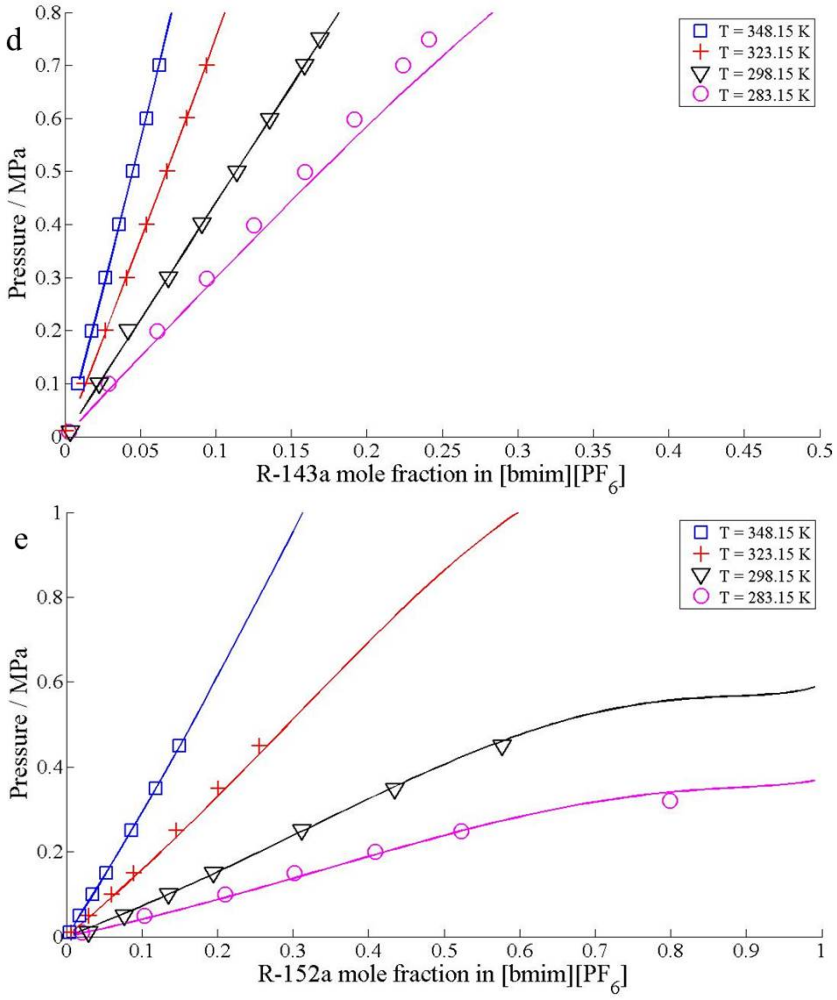

Figure 5.1 continued.

5.2.2 Effect of Absorber/Desorber Outlet Temperature on CE and η

It was previously shown in Chapter 4 that CE has a local maximum with respect to desorber outlet temperature. In this study, the CE values of five different hydrofluorocarbon refrigerants were compared, Figure 5.2. Although the five refrigerants in Figure 5.2 are all low molecular weight fluorocarbons, there is a significant difference between the CE values, regardless of desorber temperature. Four of the five refrigerants are fluorinated ethane with two (R152a), three (R143a), four (R134a), or five (R125) fluorine atoms.

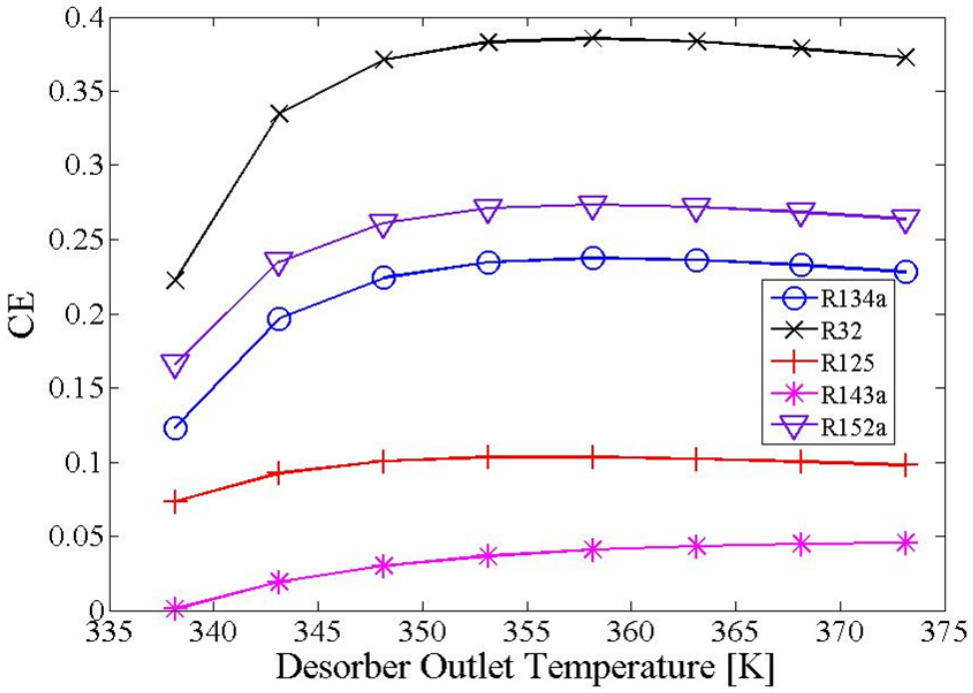

Figure 5.2: Effect of desorber outlet temperature on CE (without solution heat exchanger) at T_a= 309.65K.

R32 (difluoromethane) had the highest and R143a had the lowest CE value. Within the set of fluoroethanes, there was no trend with the degree of fluorination. However, the trend in efficiency did follow the solubility of refrigerants in [bmim][PF_6], which emphasizes the importance of refrigerant solubility in the absorbent for higher system performance. The main difference between the refrigerants was the low solubility of the refrigerant in the IL at the absorber temperature and pressure. A low solubility of the refrigerant in the IL at the absorber led to a small solubility difference between the absorber and desorber. When the solubility difference between absorber and desorber was small, larger quantities of IL had to be recirculated in the thermochemical compressor to achieve the same refrigerant flow. On each pass of the IL in the thermochemical compressor, the IL had to be heated to the desorber temperature and then cooled to the absorber temperatures, which consumes energy at the desorber.

At the lower desorber temperature values in Figure 5.2, the fluorocarbon solubility difference between the desorber and absorber became small and resulted in a lower net refrigerant flow per unit flow of the IL. CE decreased because less refrigerant was released at the desorber for each pass of the IL from the absorber to the desorber. Each pass of the IL required energy (i.e. waste heat) to heat the IL at the desorber to the highest temperature. Heat was then discharged at the absorber to lower the temperature so that the refrigerant could be absorbed there. This heating and cooling of the IL on each pass of the IL does not directly produce refrigerant vapor at the condenser, it simply brings the IL to the highest and lowest temperatures for desorption and absorption, respectively.

At higher temperature, the solubility of refrigerant in the IL at the desorber is already very low. Raising the temperature of the IL to even higher values results in only a small increase in the flow rate of the refrigerant at the exit of the desorber. The result is that additional waste heat had to be used to raise the IL temperature at the desorber with little gain in cooling capacity.

The effect of lowering the absorber temperature from 309.65K (Figure 5.2) to 300.65K is shown in Figure 5.3 for the five HFCs. When the absorber temperature was lowered nearly to that of the evaporator, 298.15K, the solubility difference between the absorber and desorber became significant even at relatively low desorber temperatures. This removes the exponential behavior at the lower temperature limit in Figure 5.2 and results in a reverse relationship of CE with respect to desorber outlet temperature. Lowering the absorber temperature to 300.65K from 309.65K resulted in an increase in CE for each of the five refrigerants. CE improved by a maximum factor of 4.2, 2.9, 3.1, 60.9, and 3.2 for refrigerants R134a, R32, R125, R143a, and R152a, respectively. This maximum effect was observed at a desorber temperature of 338.15K.

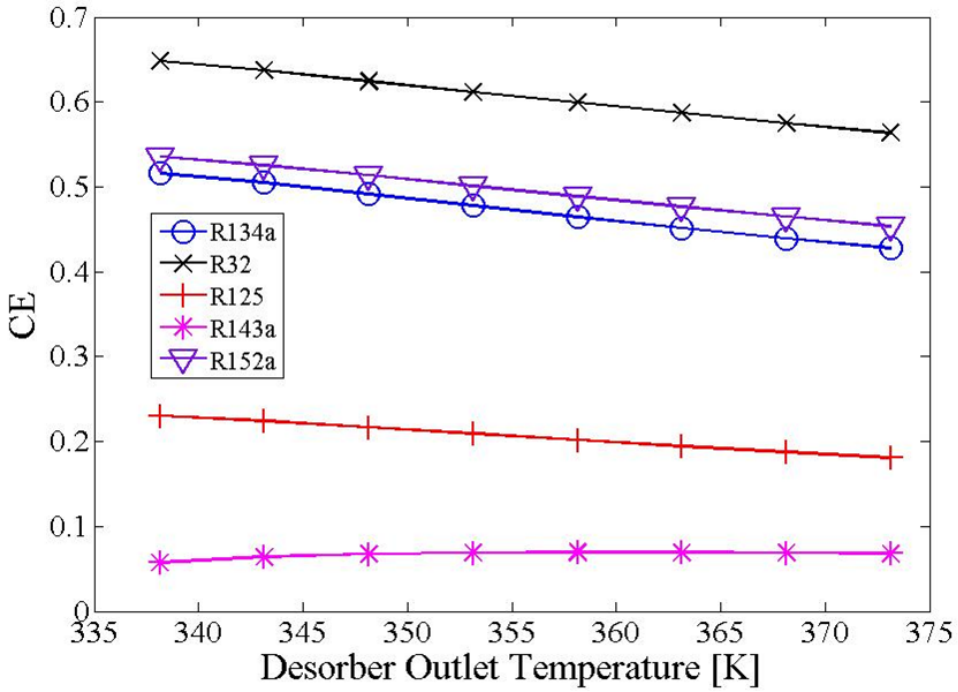

Figure 5.3: Effect of desorber outlet temperature on CE (without solution heat exchanger) at T_a= 300.65K.

The effect of desorber temperature on η was investigated for each refrigerant, as shown in Figure 5.4 for an absorber temperature of 309.65K. The coefficient of performance, η, considers only the energy to pump the IL in the thermochemical compressor and uses waste heat to drive the desorber. η increased continuously with an increase in desorber outlet temperature. This is because the net refrigerant flow passing through the evaporator per IL flow rate is the most important factor. Increasing the net refrigerant flow rate per IL flow rate lowers the pumping work. When a low grade waste heat source (~70°C) is available at the desorber, the absorber temperature becomes an important factor in achieving higher η values because of the small solubility difference

between the absorber and desorber. The maximum impact of desorber temperature was observed at 338.15K.

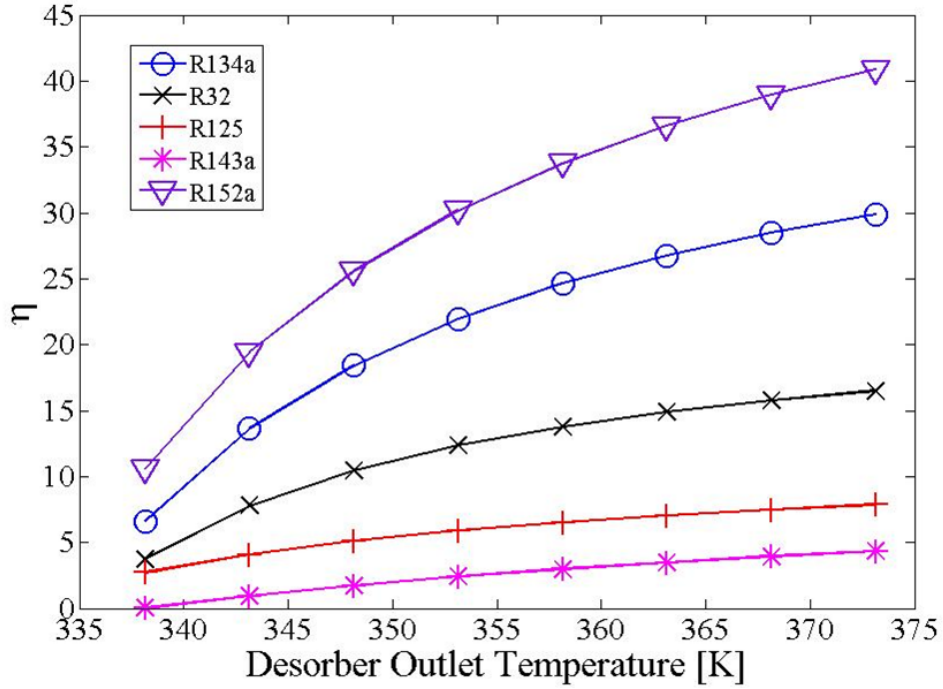

Figure 5.4: Effect of desorber outlet temperature on η (without solution heat exchanger) at T_a= 309.65K.

Lowering the absorber temperature from 309.65K to 300.65K resulted in a higher coefficient of performance, Figure 5.5. Similar to CE, η was less sensitive to desorber temperature at lower absorber temperatures because there is a larger solubility difference between the absorber and desorber when the absorber was at 300.65K. The value of η in Figure 5.5 (absorber at 300.65K) was larger than the value of η in Figure 5.4 (absorber at 309.65K) by a factor of 5.17, 3.78, 3.98, 81.3, and 4.4 for R134a, R32, R125, R143a, and R152a, respectively. The improvement factor was most dramatic for refrigerants which

have a relatively low solubility at the absorber, such as R143a in [bmim][PF_6] in this study.

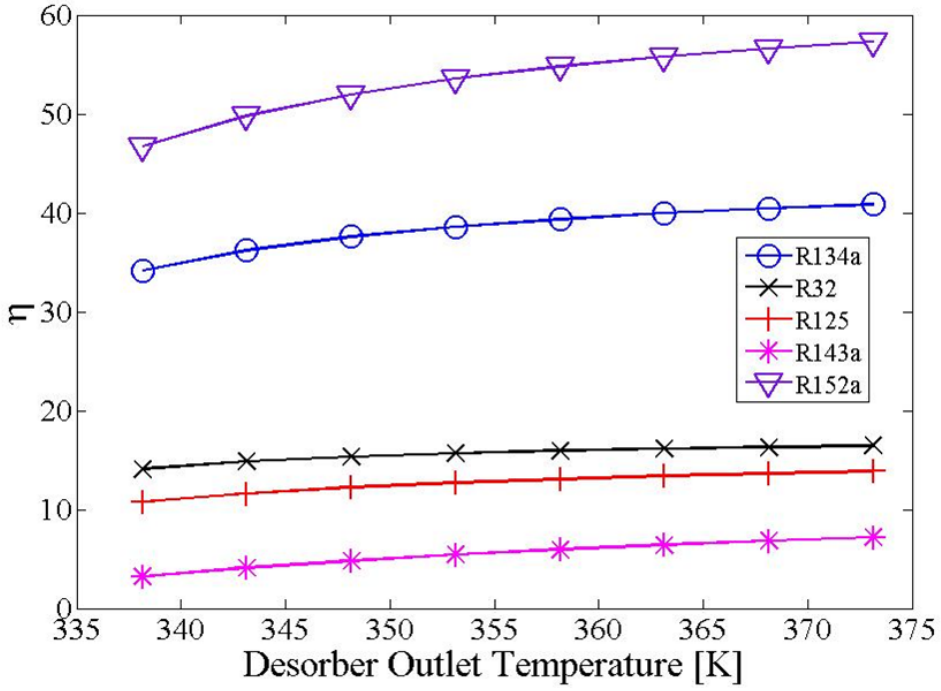

Figure 5.5: Effect of desorber outlet temperature on η (without solution heat exchanger). T_a= 300.65K.

It should be noted that the trends of refrigerant efficiencies are different between the CE (Figures 5.2 and 5.3) and COP (Figures 5.4 and 5.5). This is because the pumping work has a large effect on COP (Equation 2.14), and therefore, the pressure difference between the evaporator and condenser (ΔP) is a key parameter. Table 4.1 shows that ΔP of R32 is more than twice as large than those of R134a and R152a, which explains why R134a and R152a have a larger COP although R32 has higher solubility in [bmim][PF_6].

5.2.3 Effect of Solution Heat Exchanger on CE

The solution heat exchanger transfers heat from the strong IL solution at system point 8 to the weak IL solution at system point 6, Figure 2.2. The heat exchanger improves the system efficiency because it lowers the waste heat needed to increase the temperature of the IL in the desorber and lowers the amount of heat discharged at the absorber. Aphornratana and Sriveerakul[63] reported that an experimental 2 kW cooling capacity refrigerator showed a 60% increase in CE when three double-pipe solution heat exchangers were introduced. The CE was calculated for a system with a 25% efficiency solution heat exchanger, as shown in Figure 5.6. The weak desorber inlet solution was preheated at the adiabatic solution heat exchanger using the higher temperature strong solution leaving the desorber. 25% of the available heat was exchanged. A comparison of Figure 5.2 (CE without heat exchanger) and Figure 5.6 (CE with heat exchanger) shows that the CE increased by as much as 25%, 20%, 27%, 33%, and 22% for R134a, R32, R125, R143a, and R152a, respectively. The CE increased by a greater factor when a more efficient heat exchanger, 40% efficiency, was used. The improvement in CE was up to 47%, 37%, 52%, 66%, and 41% for R134a, R32, R125, R143a, and R152a, respectively, when the 40% efficient heat exchanger was used.

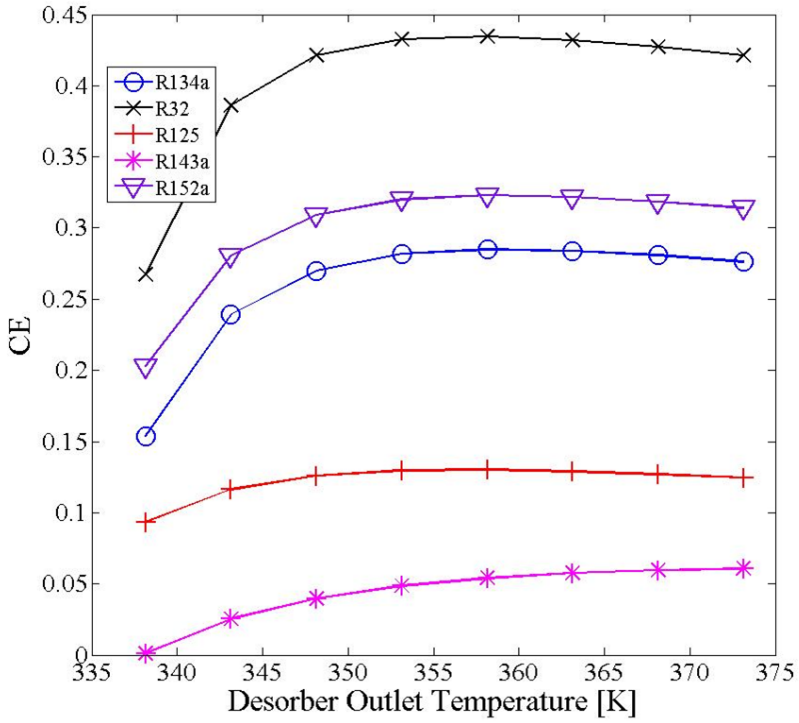

Figure 5.6: Effect of desorber outlet temperature on CE (with solution heat exchanger ε=0.25) at T_a=309.65K.

5.2.4 Effect of Pressure Drop

A potential drawback using an IL in an absorption refrigeration cycle is the friction loss during pumping the relatively high viscosity IL fluid. The pressure drop in the heat exchangers for each of the five refrigerants decreased exponentially with respect to desorber temperature, as shown in Figure 5.7. An IL with a higher refrigerant absorbance resulted in lower pressure drop and friction losses because less IL was required to deliver the same amount of cooling.

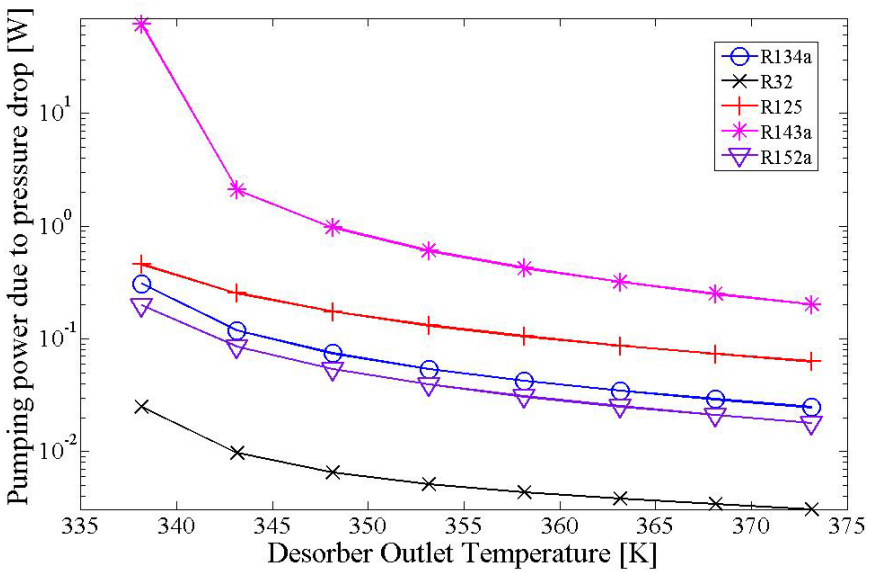

Figure 5.7: Pumping power due to pressure drop (without solution heat exchanger) at T_a =309.65K.

Refrigerants that had a relatively small solubility in [bmim][PF_6] (e.g. R143a and R125) had a relatively large pressure drop, especially at low desorber temperatures. However, even though some refrigerants had low solubility in the IL, resulting in higher pumping losses, the overall contribution of the pressure drop to the total pumping work was small for all five refrigerants. The total pumping work of the system can be calculated by Equation 4.12. Even in the case of R143a, the pumping work due to pressure drop was less than 2.5% of the total pumping work, as shown in Figure 5.8. A fraction of the pressure drop attributes from friction loss. Thus, the effect of IL viscosity is insignificant with respect to the IL pumping work.

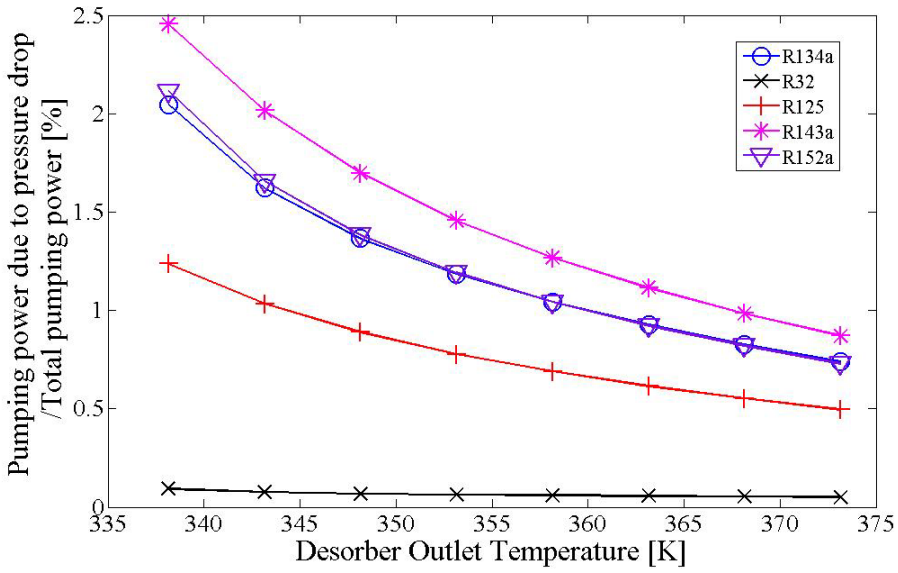

Figure 5.8: Required pumping work due to pressure drop (without solution heat exchanger) at T_a =309.65K.

5.3 Conclusion

The IL [bmim][PF_6] and five HFC refrigerants were investigated as the working fluid pairs for an absorption refrigeration system. The performance was evaluated using the Redlich-Kwong EOS and two-phase pressure drop calculations. Both CE and COP, η, had higher values at lower absorber temperatures. However, the CE response had a maximum value with respect to desorber temperature, depending on the absorber temperature. The trends between solubility and performance stated in this work provide useful guidance in the operation and efficiency of IL-based absorption refrigeration systems for cases where limited waste heat (CE) or excess waste heat (η) are available. The working fluid pairs showed an excellent COP, η, when waste heat was used to drive the desorber. The introduction of a solution heat exchanger improved the system

performance by lowering the amount of heat required at the desorber and minimizing the heat discharged at the absorber. The pumping loss due to friction effects during pumping of the IL was small and insignificant with respect to the total pumping energy.

CHAPTER 6

COMPARISON STUDY BETWEEN R134/[bmim][PF_6] AND R134a/[bmim][PF_6] WORKING FLUIDS

6.1 Introduction

The analysis presented in Chapter 5 showed 1,1,1,2-tetrafluoroethane (R134a) to be a promising refrigerant when paired with [bmim][PF_6] as the working fluid for a waste heat recycling absorption refrigeration system. 1,1,2,2-tetrafluoroethane (R134), an isomer of R134a, was expected to have similar results with that of R134a. However, the shift in fluorine substitution (1,1,1,2-tetrafluoroethane to 1,1,2,2-tetrafluoroethane) has resulted in a significant change in the absorption of the fluorocarbon in [bmim][PF_6] and the resulting performance of the absorption refrigeration system. In this chapter, the performance of the R134/[bmim][PF_6] working fluid pair was also modeled using a two-phase pressure drop and Equation-of-State (EOS) model. The effects of a counter-flowing solution heat exchanger, desorber temperature, and absorber temperature on the system performance were evaluated. Computational results of R134/[bmim][PF_6] were compared with that of R134a/[bmim][PF_6].

6.2 Results and Discussion

6.2.1 System Parameters

The change in fluorine position in tetrafluoroethane from the first carbon to the second carbon (R134a is 1,1,1,2-tetrafluoroethane and R134 is 1,1,2,2-tetrafluoroethane) has little effect on its physical properties, such as density, and boiling point. However,

this difference in chemical structure has a significant effect on its interaction with [bmim][PF_6], which affects the performance of the absorption refrigeration cycle. The solubility of R134 in the IL absorbent was predicted using the two phase pressure drop EOS model, Figure 6.1. The calculated values are in good agreement with the experimentally measured data reported by Shiflett and Yokozeki[64]. The BIPs found for R134/[bmim][PF_6] mixture are shown in Table 6.1. In Figure 6.1, the experimentally determined values are the data points and the solid lines correspond to the fitted values. Surprisingly, R134 showed significantly higher solubility at the same temperature and pressure in comparison to R134a at the same temperatures, Figure 5.1(a). This is most likely due to the higher probablity for hydrogen bonding between the symmetrical R134 and [bmim][PF_6][48].

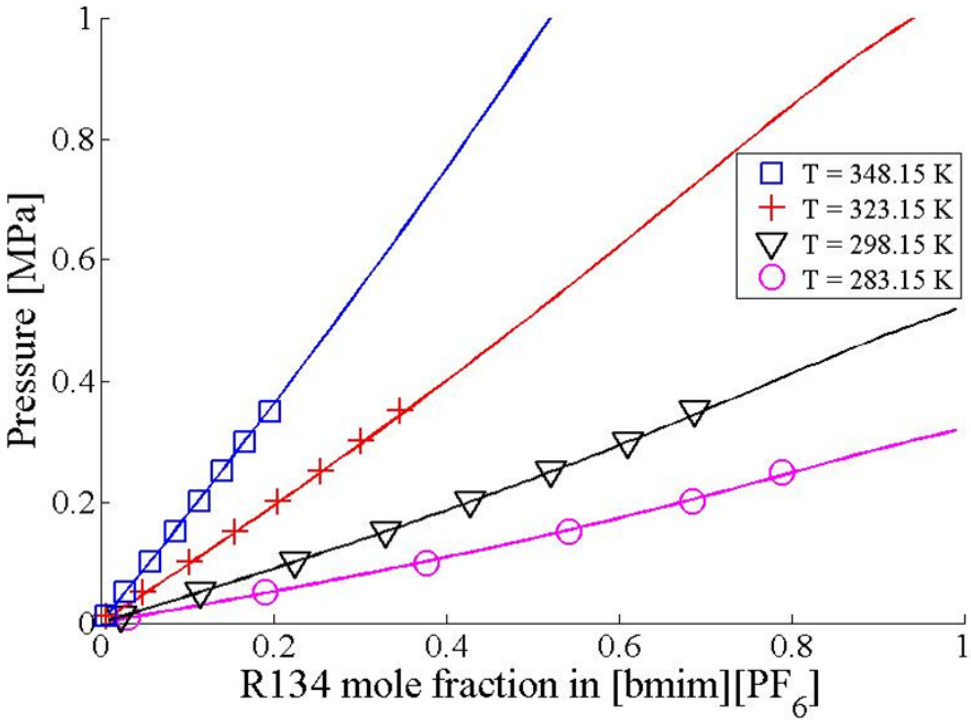

Figure 6.1: R134 solubility in [bmim][PF_6] as a function of temperature [K] and pressure [MPa]. Symbols: experimental solubility data[64]; lines: computed EOS model.

Table 6.1: Binary interaction parameters (BIPs) for R134 and [bmim][PF_6].

Fluid pair	$l_{12} = l_{21}$	k_{12}	τ_{12} **(K)**	ΔP**(MPa)**[a]
R134/[bmim][PF_6]	0.0418	-0.0451	24.4896	0.002

[a]Standard deviations of non-linear least squares in pressures.

The operating pressure of the system is determined by the saturated pressure of the refrigerant. The vapor pressure of R134 and R134a at the condenser and evaporator temperature of 50°C and 25°C, respectvely, are listed in Table 6.2. The critical properties along with β values and coefficients for ideal gas heat capacity of R134 are summarized in Table 6.3 and 6.4, respectively.

Table 6.2: Vapor pressure of R134[64] and R134a [kPa][29].

Temperature [K]	**R134**	**R134a**
298.15	526.0	664.9
323.15	1062.9	1318.6

Table 6.3: EOS constants of R134.

Pure compound	T_c **(K)**	P_c **(kPa)**	β_0	β_1	β_2	β_3
R134[13]	391.97	4641	1.0012	0.48291	-0.05070	0

Table 6.4: Coefficients for ideal gas heat capacity of R134 [J·mol^{-1}].

Pure compound	C_p^0 **(J·mol^{-1})**	C_p^1 **(J·mol^{-1}K^{-1})**	C_p^2 **(J·mol^{-1}K^{-2})**	C_p^3 **(J·mol^{-1}K^{-3})**
R134[34]	15.58	0.28694	-2.028×10^{-4}	5.39633×10^{-8}

6.2.2 Effect of Absorber/Desorber Outlet Temperature on CE

The effect of changing several key operating conditions was evaluated using the model developed in this work. The effect of lowering the absorber temperature from 309.65K to 300.65K was evaluated. Figure 6.2 shows the value of CE for the absorber at 309.6K and Figure 6.3 shows the resulting value of CE for the absorber at 300.65K. For both absorber temperatures and in the range of desorber temperatures R134 showed superior CE than that of R134a. The CE value was generally observed to increase when the absorber temperature was lowered from 309.65K to 300.65K due to higher refrigerant solubility in the absorber. R134 had a higher CE value than R134a at the same temperature, with an average improvement of 32.3% and 92.3% for the absorber operated at 300.65K and 309.65K, respectively. This larger difference in CE values between the refrigerants at 309.65K is due to the higher solubility of R134 compared to R134a. The effect of solubility on the system efficiency becomes increasingly important for cases where the solubility difference between the absorber and desorber is small (i.e. high absorber temperature).

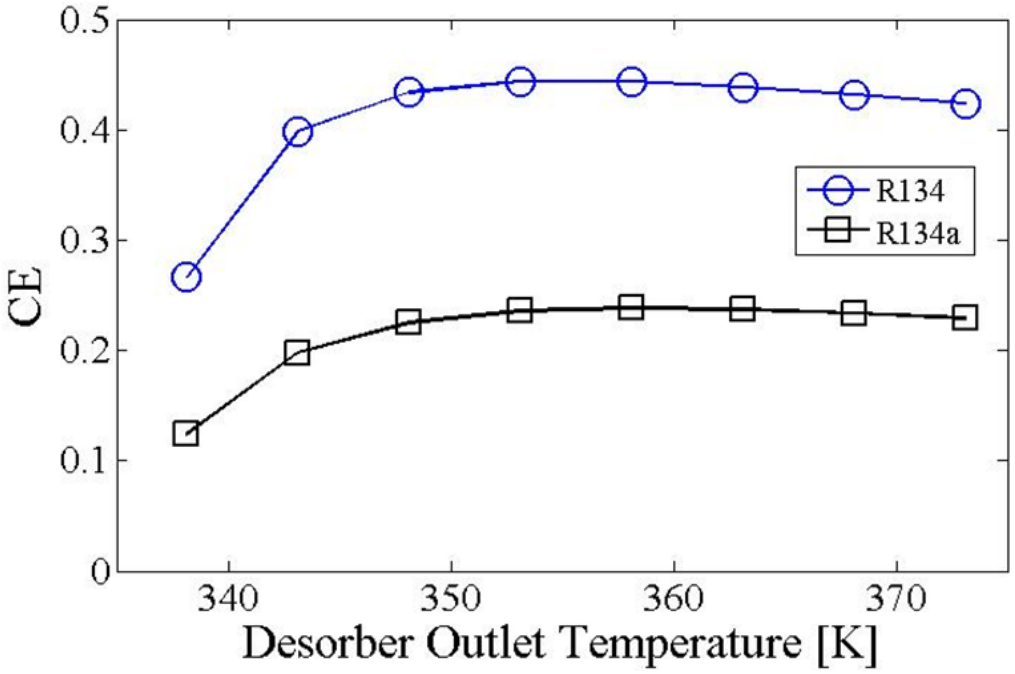

Figure 6.2: Effect of desorber outlet temperature on CE (without solution heat exchanger) at T_a= 309.65K.

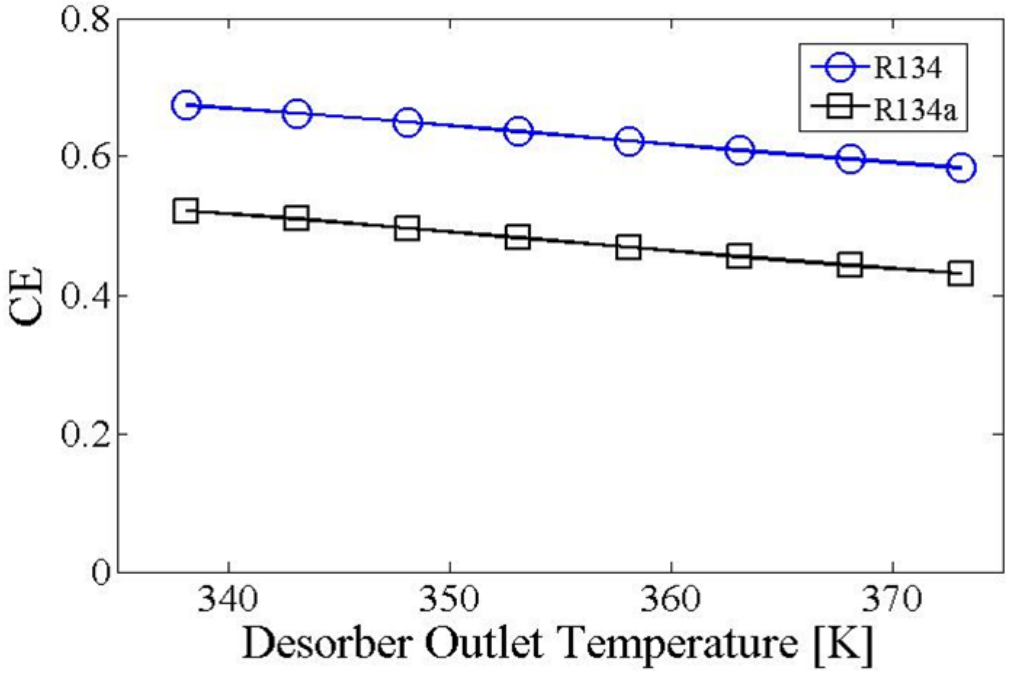

Figure 6.3: Effect of desorber outlet temperature on CE (without solution heat exchanger) at T_a= 300.65K.

6.2.3 Effect of Solution Heat Exchanger on CE

As mentioned in Chapter 5, the introduction of a solution heat exchanger between the inlet and outlet of the desorber improves the performance of the cycle. A 35% efficient heat exchanger improved the CE values by 16.4% and 32.6% in average for R134 and R134a (see Figure 6.4), respectively, compared to the case without the heat exchanger as shown in Figure 6.2. The system performance was enhanced to a greater extent for the refrigerant with lower CE values, R134a.

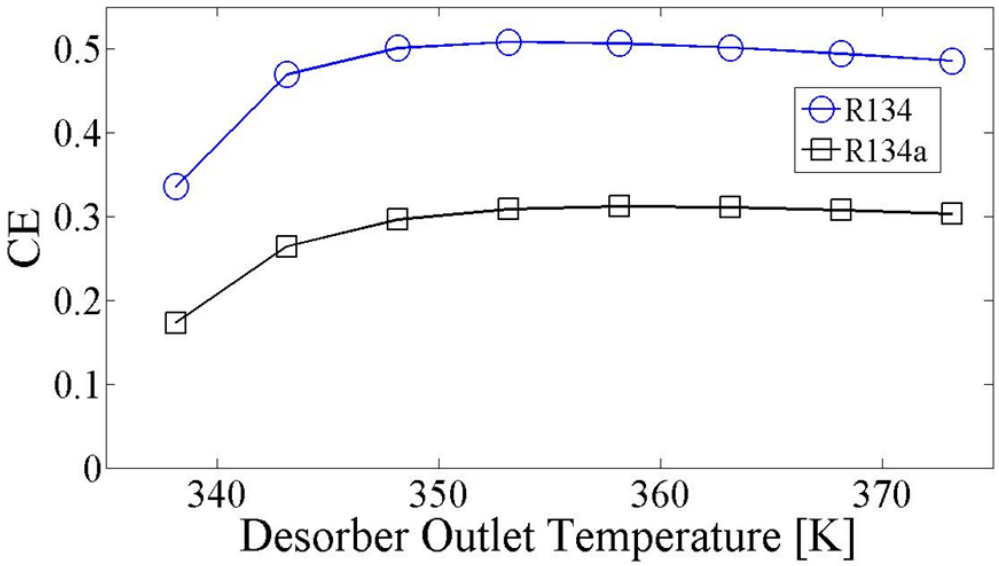

Figure 6.4: Effect of desorber outlet temperature on CE (with solution heat exchanger ε=0.35) at T_a=309.65K.

6.2.4 Effect of Absorber/Desorber Outlet Temperature on η

The coefficient of performance η is plotted with respect to desorber outlet temperature in Figures 6.5 and 6.6 for absorber temperatures of 309.65K and 300.65K, respectively. At higher desorber outlet temperatures, the pumping work was reduced due to an increase in the refrigerant-to-absorbent circulation ratio. This means that the IL absorbent can carry more refrigerant on each pass which leads to an efficiency increase. The liquid pumping work is the product of the liquid volumetric flow rate and pressure difference between the absorber and desorber: $W_p = \dot{V}_l \times \Delta P$. Therefore, when free, waste-heat is used at the desorber to drive the system, the operating pressure range and solubility difference between the absorber and desorber are both important because the goal is to minimize the pumping work by reducing the amount of IL pumped. Both refrigerants had higher COP values at lower absorber temperature due to the higher refrigerant-to-absorbent ratio resulting in a lower liquid volumetric flow rate. The R134/IL pair had twice (Figure 6.6) or three times (Figure 6.5) the efficiency of the R134a/IL pair depending on the absorber temperature. The improvement by replacing R134a/IL with R134/IL is greater for the COP values than it is for CE because the pumping work, W_p, which dominates COP is two orders of magnitude smaller than the heat required at the desorber (Q_d) and absorber (Q_a). W_p is the only term in the denominator for computing COP. The R134/IL pair had less pumping work than the R134a/IL pair due to several thermophysical properties including: (i) larger molar enthalpy of vaporization (Table 6.5); (ii) smaller operating pressure range (Table 6.2); (iii) larger solubility and solubility difference in [bmim][PF_6] (smaller liquid volumetric flow); and (iv) larger liquid density (Table 6.5).

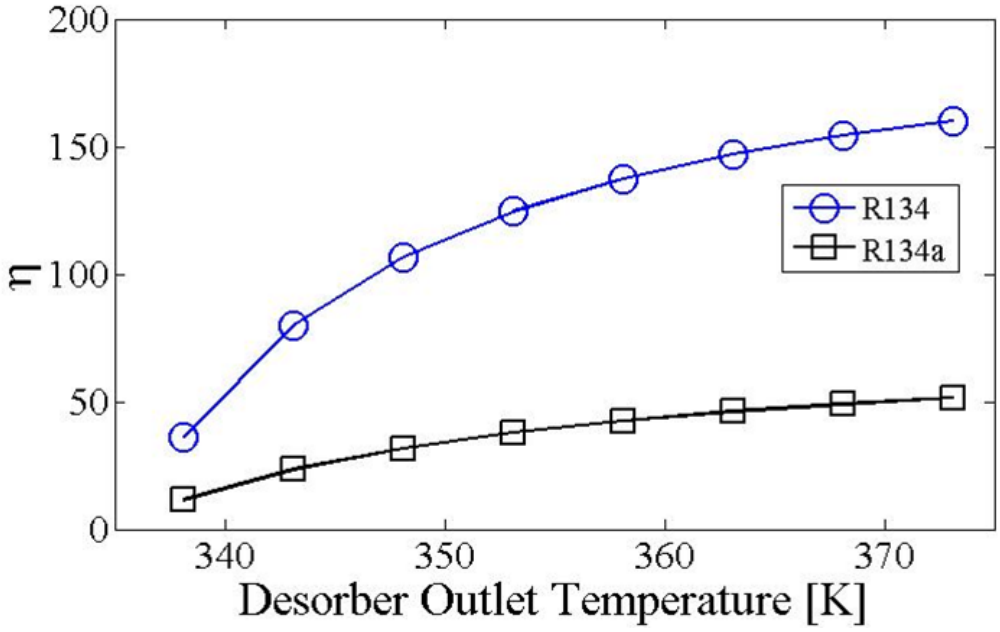

Figure 6.5: Effect of desorber outlet temperature on η (without solution heat exchanger) at T_a= 309.65K.

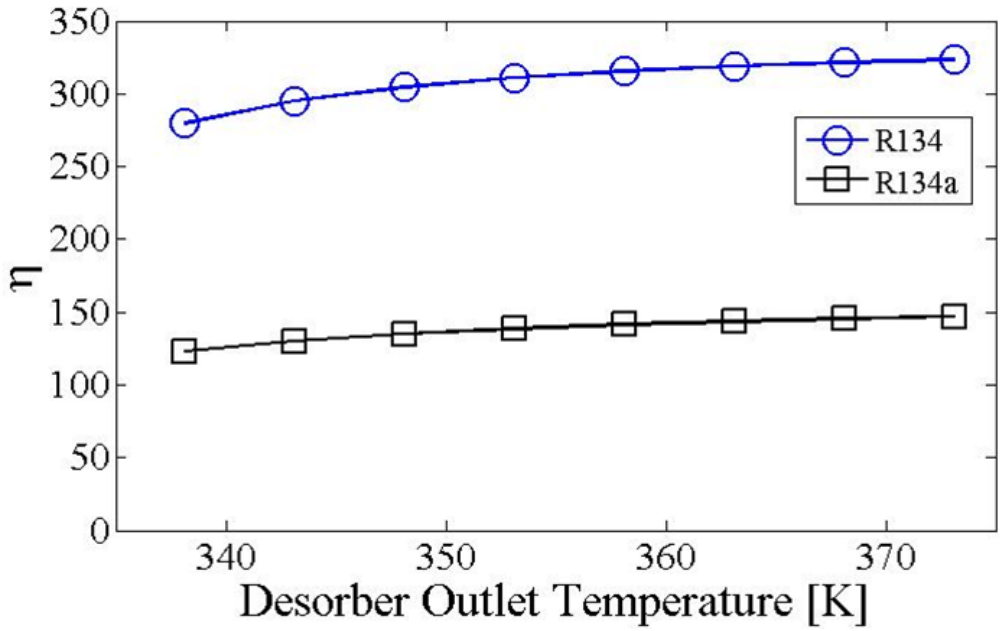

Figure 6.6: Effect of desorber outlet temperature on η (without solution heat exchanger) at T_a= 300.65K.

Table 6.5: Enthalpy of vaporization (ΔH_{vap}) and saturated liquid density (ρ) values of R134 and R134a at 298.15K.

	$\Delta H_{vap}^{29,65}$ [kJ/mol]	$\rho^{29,66}$ [g/cm^3]
R134	16.33	1.290
R134a	14.64	1.207

6.3 Conclusion

The R134/[bmim][PF_6] fluid pair was evaluated in an energy recycling absorption refrigeration system. The EOS model showed that R134 had higher solubility difference in [bmim][PF_6] than R134a in the same IL at the cooling cycle operating conditions, which resulted in higher CE values. The larger molar enthalpy of vaporization, smaller operating pressure range, and larger liquid density of R134 compared to R134a also contributed to the improvement in COP values.

CHAPTER 7

ANALYSIS OF [hmim][PF_6] AND [hmim][Tf_2N] AS ABSORBENTS

7.1 Introduction

Refrigerant solubility in an IL tends to increase with longer alkyl-groups most likely due to larger free volume[67]. Ren and Scurto reported that for the solubility of R134a, switching the anions showed a more pronounced effect compared to that of increasing the alkyl chain length of the cation[47]. The solubility of R134a increased in the order of $[BF_4]^-$<$[PF_6]^-$<<$[Tf_2N]^-$ with the same cation, 1-hexyl-3-methylimidazolium ($[hmim]^+$).

The focus of this work is the effect of IL selection in the performance of an absorption refrigeration system. Two ILs, each with excellent solubilities were selected as the test case: the bis(trifluoromethylsulfonyl)imide ($[Tf_2N]^-$) and hexafluorophosphate ($[PF_6]^-$) anions with the common $[hmim]^+$ cation. The systematic analysis will provide a guideline for selecting a suitable IL for absorption refrigeration among the variety of available ILs. The effect of a counter-flowing solution heat exchanger, desorber temperature, and absorber temperature on the system performance was evaluated. Also the effect of IL viscosity has been evaluated using a two-phase pressure drop Equation-of-State (EOS) model.

7.2 Results and Discussion

7.2.1 System Parameters

R134a has high solubility in both [hmim][PF_6] and [hmim][Tf_2N], as shown in Figures 7.1 and 7.2. In particular, at a low temperature, 298.15K, the solubility values are nearly similar, however, at higher temperatures, the [hmim][Tf_2N] IL shows a higher absorption capacity for R134a. The magnitude of the absorbance at high temperature is important to minimize the circulation ratio of the solution (α). The required mass flow rate of IL (m_{IL}) to deliver a given cooling capacity can be expressed in terms of the mass flow rate of the refrigerant (m_r), as shown in Equation 7.1.

$$m_{IL} = \frac{(1-x_w)(1-x_s)}{(x_w - x_s)} m_r \tag{7.1}$$

Therefore, the absorbent IL should have large overall solubility of the refrigerant (x_w and x_s) and a large solubility difference between the two temperatures in order to minimize the amount of working fluid in the system which has to be recirculated and heated and cooled, in order to improve the system efficiency. Equation 7.1 shows that when the solubility of the refrigerant is sensitive to temperature, the IL with a low overall solubility at high temperature and pressure has a significant advantage. The EOS constants, BIP values, coefficients for ideal gas heat capacity of the pure compounds used in this work are summarized in Table 7.1 through 7.3.

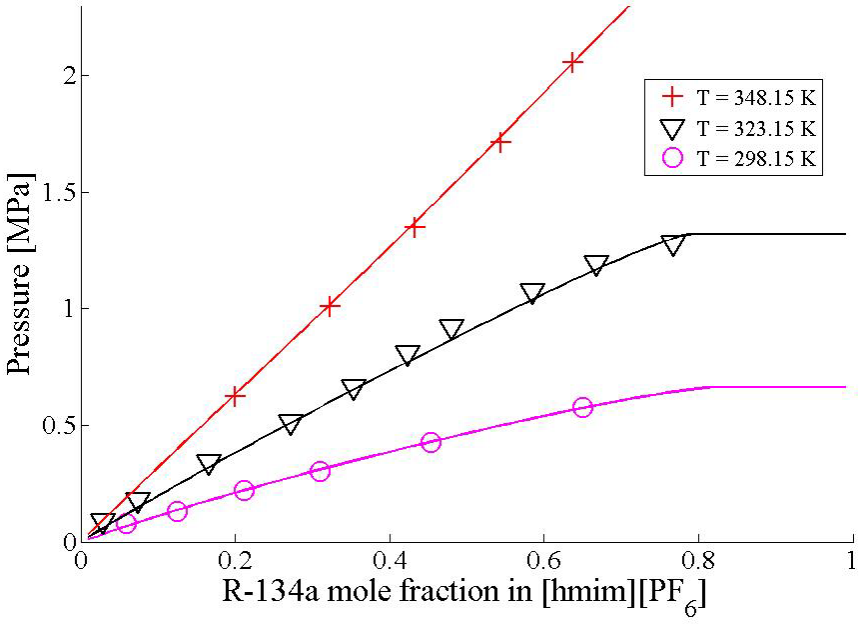

Figure 7.1: R134a solubility in [hmim][PF_6] as a function of temperature (K) and pressure (MPa). Symbols: experimental solubility data[47]; lines: computed EOS model.

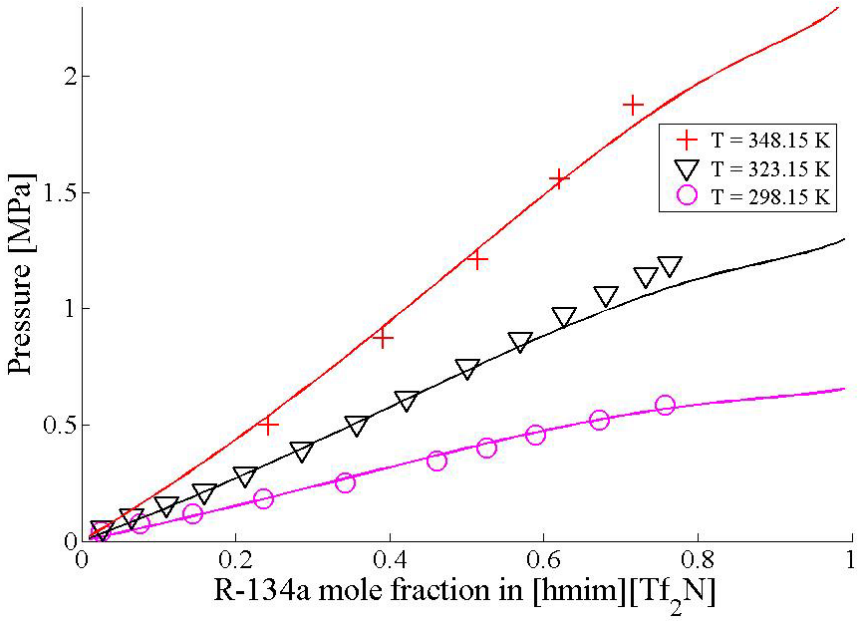

Figure 7.2: R134a solubility in [hmim][Tf_2N] as a function of temperature (K) and pressure (MPa). Symbols: experimental solubility data[47]; lines: computed EOS model.

Table 7.1: EOS constants of R134a, [hmim][PF_6], and [hmim][Tf_2N].

Pure compound	T_c **(K)**	P_c **(kPa)**	β_0	β_1	β_2	β_3
R134a[34]	374.21	4059	1.0025	0.50532	0.04983	0
[hmim][PF_6]	754.3[47]	1550[47]	1.0	2.1132	0	0
[hmim][Tf_2N][68]	815.0	1611	1.0012	0.50036	0	0

Table 7.2: Binary interaction parameters for [hmim][PF_6]/ R134a and [hmim] [Tf_2N]/R134a.

Fluid pair	$l_{12} = l_{21}$	k_{12}	τ_{12} **(K)**	**AAD[a] (%)**
[hmim][PF_6]/ R134a	-0.0659	0.0559	-1.6593	4.87
[hmim][Tf_2N]/ R134a	0.0233	-0.0116	-9.0682	8.13

[a]average absolute relative deviation of fit in pressure.

Table 7.3: Coefficients for ideal gas heat capacity of pure compounds [J·mol^{-1}].

Pure compound	C_p^0 **(J·mol^{-1})**	C_p^1 **(J·mol^{-1}K^{-1})**	C_p^2 **(J·mol^{-1}K^{-2})**	C_p^3 **(J·mol^{-1}K^{-3})**
R134a[34]	12.89	0.30500	-2.342×10^{-4}	6.852×10^{-8}
[hmim][PF_6][69]	-42.465	1.49781	-10.120×10^{-4}	24.994×10^{-8}
[hmim][Tf_2N][69]	-46.914	1.88368	-12.953×10^{-4}	31.963×10^{-8}

7.2.2 Effect of Absorber/Desorber Outlet Temperature on CE

It was previously shown that CE has a local maximum with respect to desorber temperature where the solubility of the refrigerant is the limiting factor of the absorption system. This is also the case for [hmim][PF_6]/R134a and [hmim][Tf_2N]/R134a mixtures, as shown in Figure 7.3. However, in previous studies where [bmim][PF_6] was paired with 6 different hydrofluorocarbon refrigerants (R125, R134a, R134, R143a, R152a, and R32), the CE curves did not cross each other. In other words, the working pairs that showed higher efficiency at one specific operating condition also had higher efficiency under a wide range of conditions. On the other hand, [hmim][Tf_2N] had a lower CE than that of [hmim][PF_6] when the absorber and desorber temperatures were set to 308.15K and 337.15K, respectively. However, [hmim][Tf_2N] had a higher CE when the desorber temperature increased. This is because the solubility of R134a in [hmim][Tf_2N] was still relatively high at the desorber temperature of 337.15K. Due to the higher operating pressure at the desorber, the solubility at the desorber was only slightly lower compared to that of the absorber. Therefore, large amount of IL was required to deliver 100 W of cooling at the evaporator resulting in more sensible heating during recirculation of the IL. At a lower absorber temperature of 300.65K, the CE decreased with respect to desorber temperature, as shown in Figure 7.4. Regardless of the curvature in the CE vs desorber plot, the CE values nearly doubled by lowering the absorber temperature as a result of the higher solubility difference between the absorber and desorber.

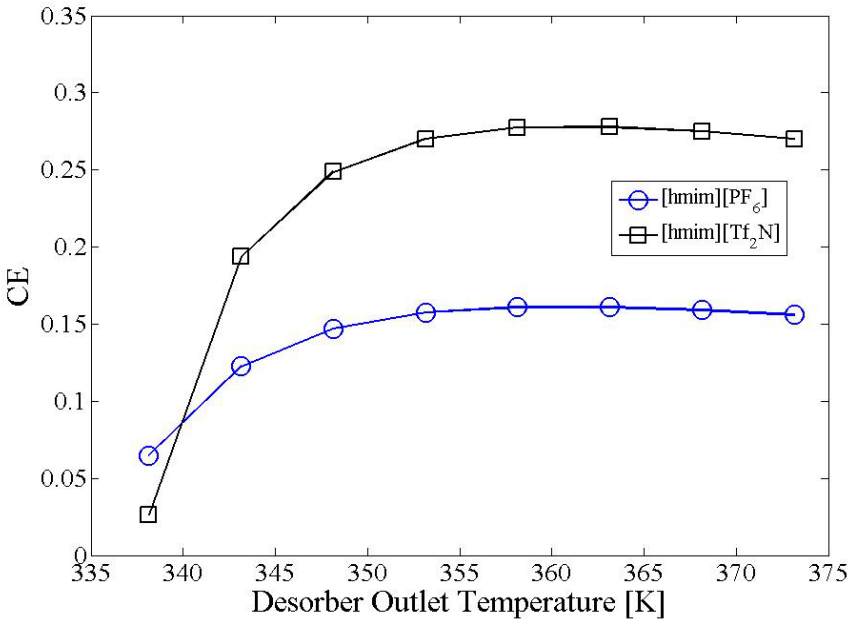

Figure 7.3: Effect of desorber outlet temperature on CE (without solution heat exchanger) at T_a= 308.15K.

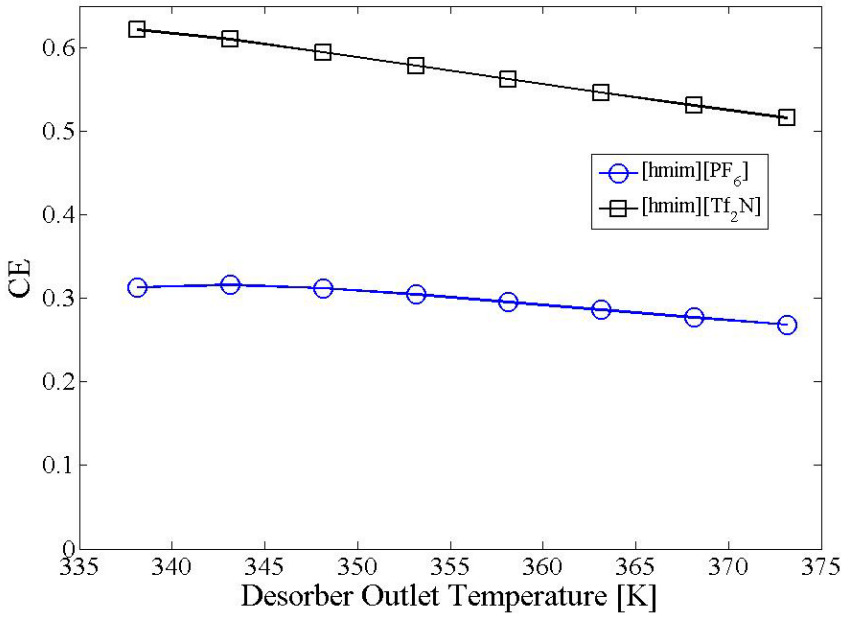

Figure 7.4: Effect of desorber outlet temperature on CE (without solution heat exchanger) at T_a= 300.65K.

7.2.3 Effect of Solution Heat Exchanger on CE

Introducing a solution heat exchanger increased the CE values due to the lowered Q_d term by preheating the working fluids at the desorber inlet, Figures 7.5 and 7.6. Note that the efficiency of [hmim][Tf_2N] more than doubled by utilizing the solution heat exchanger when the absorber temperature was 308.15K and the desorber temperature was near the lower boundary (337.15K and 343.15K), as shown in Figures 7.3 and 7.5. As previously stated, these conditions are close to the operating limit where the solubility difference between the absorber and desorber nearly converge. Accordingly, a significant amount of IL is circulated in the system to provide the same amount of net refrigerant flow at the evaporator, which requires additional sensible heating at the desorber (Q_d) and cooling at the absorber (Q_a). With the introduction of a solution heat exchanger, the magnitude of both Q_d and Q_a are lowered and thus the system efficiency was improved. Although the CE is higher when the absorber temperature is lowered from 308.15K (Figure 7.5) to 300.65K (Figure 7.6), [hmim][Tf_2N] has considerably high CE even when the absorber temperature was at 308.15K with a maximum of 0.542. Therefore, the [hmim][Tf_2N]/R134a working fluid pair has a beneficial operating condition because the cooling at the absorber is minimized.

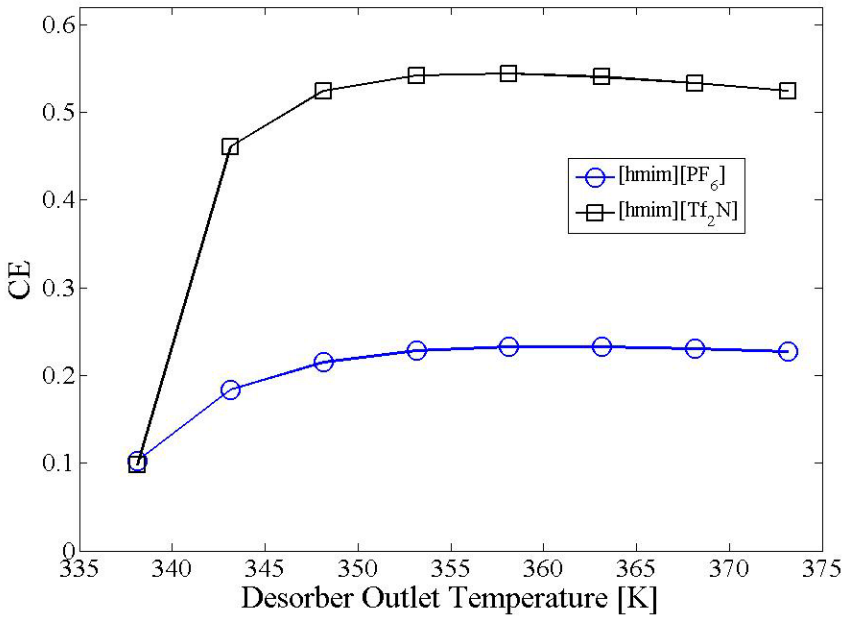

Figure 7.5: Effect of desorber outlet temperature on CE (with solution heat exchanger, ε=0.8) at T_a=308.15K.

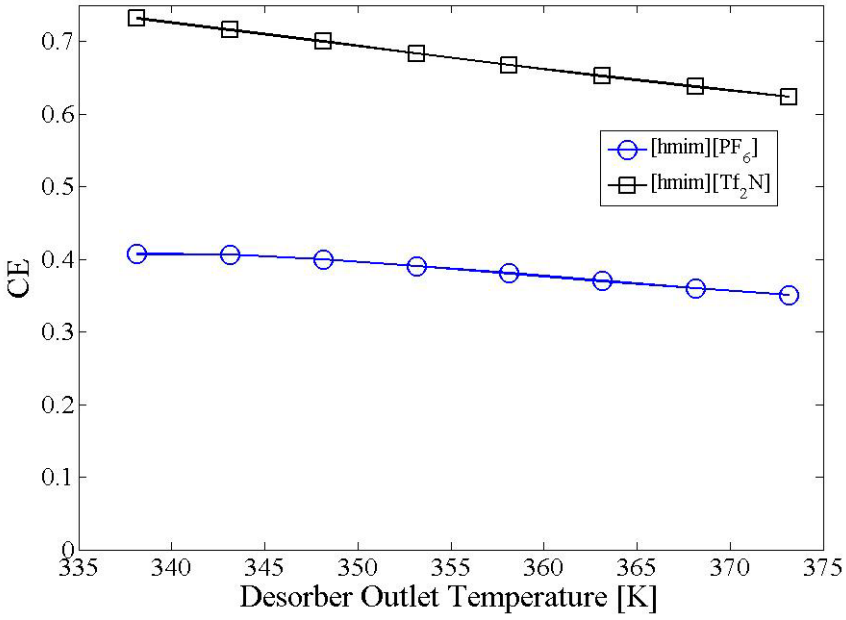

Figure 7.6: Effect of desorber outlet temperature on CE (with solution heat exchanger, ε=0.8) at T_a=300.65K.

7.2.4 Effect of Absorber/Desorber Outlet Temperature on η

The coefficient of performance (η) is plotted with respect to desorber outlet temperature in Figures 7.7 and 7.8 for absorber temperatures of 308.15K and 300.65K, respectively. At higher desorber outlet temperatures, the pumping work was reduced due to an increase in the refrigerant-to-absorbent circulation ratio. Both ILs had higher COP values at lower absorber temperature due to lower liquid volumetric flow rate. At high absorber temperature, the COP values for the two ILs are similar, as shown in Figure 7.7. The key factor that determined the COP is the solubility values at the absorber and desorber because the refrigerant operating pressures are fixed by the vapor pressure of R134a. Both CE and COP show the same trend at high absorber temperature, 308.15K. The efficiency of [hmim][PF_6] was higher at the lower desorber temperature range, but the values of [hmim][Tf_2N] exceeded that of [hmim][PF_6] as the desorber temperature was increased. When there was a significant solubility difference between the absorber and desorber, [hmim][Tf_2N] showed an average of 70% higher COP than that of [hmim][PF_6], as shown in Figure 7.8.

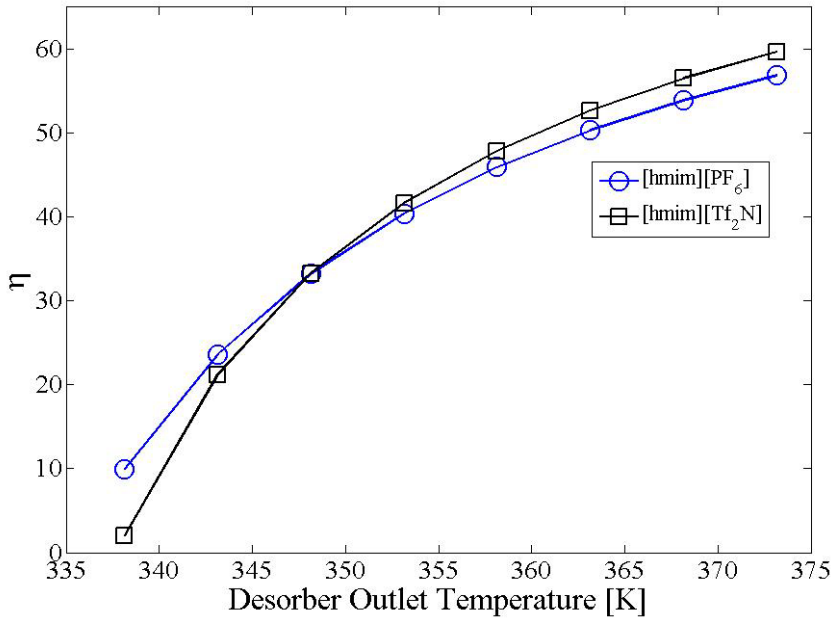

Figure 7.7: Effect of desorber outlet temperature on η at T_a= 308.15K.

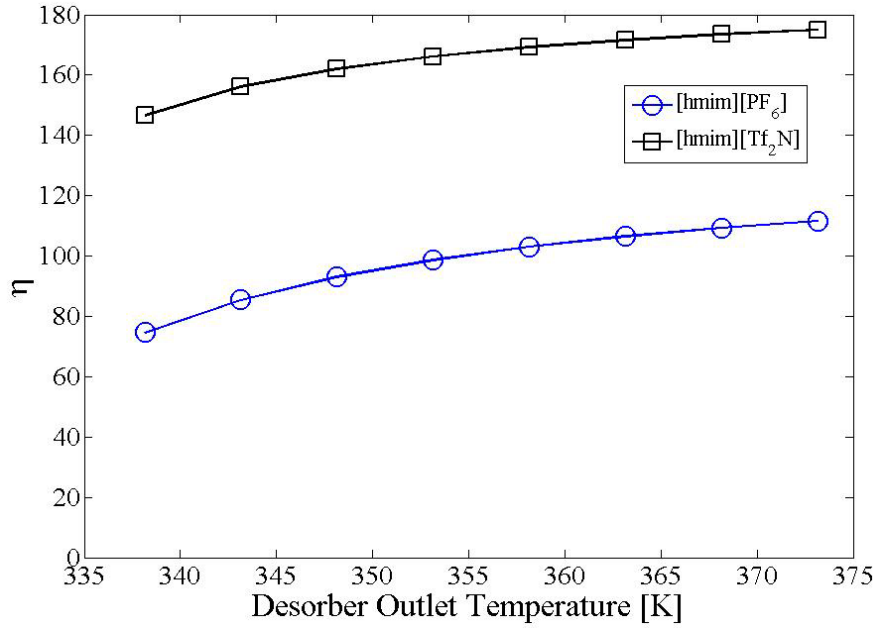

Figure 7.8: Effect of desorber outlet temperature on η. T_a= 300.65K.

7.2.5 Effect of Viscosity on Pressure Drop

The viscosity of [hmim][Tf_2N] is approximately 7 times less than that of [hmim][PF_6] at 298.15K[70]. As R134a reaches its solubility limit in [hmim][Tf_2N] under certain conditions, the effect of lower viscosity but higher circulation ratio was explored. The required pumping work due to pressure drop is plotted in Figure 7.9 with respect to desorber temperature for an absorber temperature of 308.15K. The viscosity of the IL/R134a mixture decreased as the fraction of R134a increased, which results in a decrease in the pumping work due to pressure drop with respect to desorber temperature. For both ILs, less than 4% of the total pumping power was attributed due to pressure drop and therefore, an even smaller fraction is contributed by friction loss. At a desorber temperature of 337.15K, [hmim][Tf_2N] has slightly higher pumping power than that of [hmim][PF_6] due to the larger quantity of IL. The pumping power due to pressure drop of [hmim][Tf_2N] showed a sharp decrease at higher desorber temperatures, although the effect on the total pumping power was trivial.

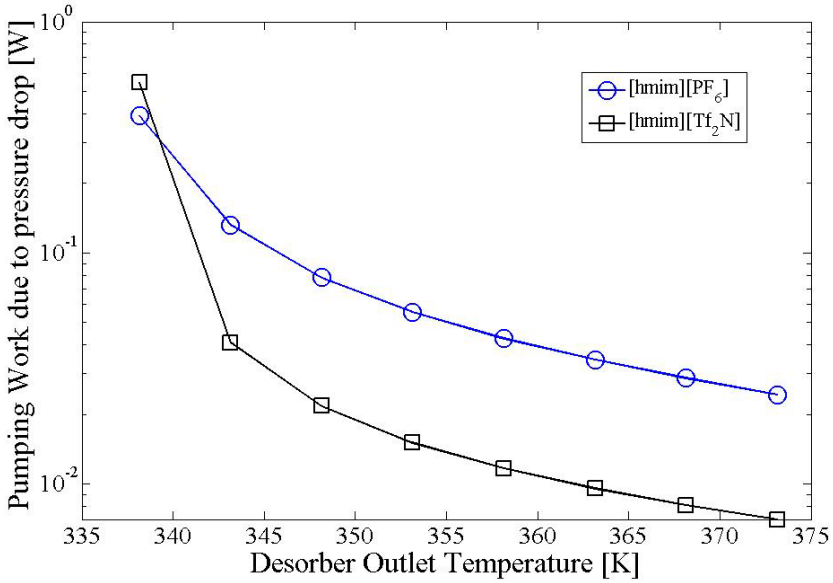

Figure 7.9: Pumping power due to pressure drop (without solution heat exchanger) at T_a =308.15K.

7.2.6 Effect of the IL Anion on the Absorption Refrigeration System Performance

R134a has high solubility in both ILs, [hmim][PF_6] and [hmim][Tf_2N], due to the hydrogen bonding between the terminal protons of the refrigerant and electron donating groups of the anion of the ILs [71]. The presence of electronegative moieties (F, N, and O) in the $[Tf_2N]^-$ anion explains the high solubility of R134a in the [hmim][Tf_2N] over a wide range of temperatures. When a high temperature heat source is available at the desorber, using an IL with the high overall refrigerant solubility is advantageous because large x_w and x_s values will result in a minimum quantity of working fluid per cooling capacity, Equation 7.1. However, when the temperature difference between the absorber and desorber is not large (small denominator term in Equation 7.1), a higher overall refrigerant solubility may not always lead to higher system performance.

7.3 Conclusion

[hmim][Tf_2N] had higher CE and COP in most conditions when compared to those of [hmim][PF_6]. Because of the high overall solubility of R134a in [hmim][Tf_2N], [hmim][PF_6] showed higher efficiency in cases in which the absorber temperature was relatively high and the desorber temperature was low. When waste heat is limited and heat needs to be supplied to the desorber, introducing a solution heat exchanger can significantly improve the CE of [hmim][Tf_2N]. The viscosity of [hmim][Tf_2N] was 7 times less than that of [hmim][PF_6], but the effect to the whole system performance and total pumping work was found to be small.

CHAPTER 8

EXPERIMENTAL BENCH-TOP SYSTEM

8.1 System Description

In this study, an experimental setup for a laboratory scale absorption refrigeration system using IL based working fluids has been built and operated for the first time, Figure 8.1. The microfluidic channel heat/mass exchangers were fabricated in copper and used for an evaporator, a condenser, an absorber, and a desorber. A magnetic gear pump was employed for the circulation of the HFC/IL mixture. A 150 ml stainless-steel cylinder was installed for the separation of refrigerant-vapor from the mixture. Vapor/non-condensables were trapped in the 50 ml liquid-receiver located at the outlet of the condenser to guarantee liquid flow through the expansion device. Orifice-type metering valves were adopted for the expansion devices for fine adjustment of flow rates, as well as the system cooling capability. Kapton heaters were attached on the backsides of the evaporator and desorber to simulate the heat dissipation from chip, and waste-heat as an energy source, respectively. The absorber and the condenser were cooled by secondary water loops. Pressure transducers were placed at the inlet and outlets of the evaporator, absorber, desorber, condenser, and at the separator mixture outlet. The temperatures at the inlets and outlets of all components were measured using T-type (copper-constantan) thermocouples. The heat/mass exchangers, the separator and the liquid-receiver were insulated using fiberglass insulation. The copper tubes (¼ in. diameter) were thermally insulated using elastomeric material (ethylene propylene terpolymer). As shown in Figure 8.4, the heat/mass exchangers have microchannels with

1×1 mm cross-sectional area and the channel pitch of 1.5 mm. The evaporator and condenser have channel lengths of 2 cm and 3 cm, respectively, while the absorber and desorber have the channel lengths of 8 cm. The relatively large cross-sectional area of the absorber and the desorber allowed a lower pressure drop due to the high viscosity of ILs.

The experimental system is constructed based on the layout described in the schematic system diagram in Figure 2.2, except for the elimination of the solution heat exchanger ($\varepsilon=0$).

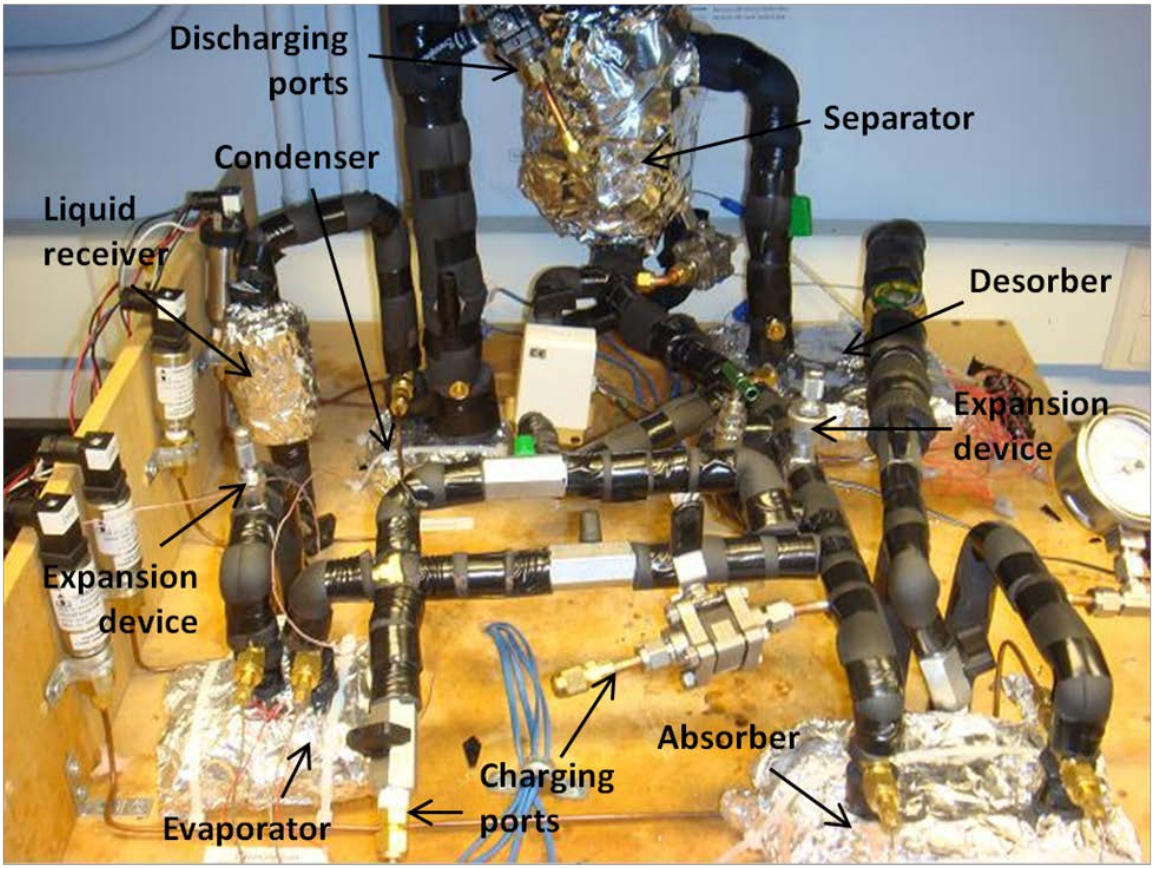

Figure 8.1: Experimental test setup for absorption refrigeration system using IL based working fluid.

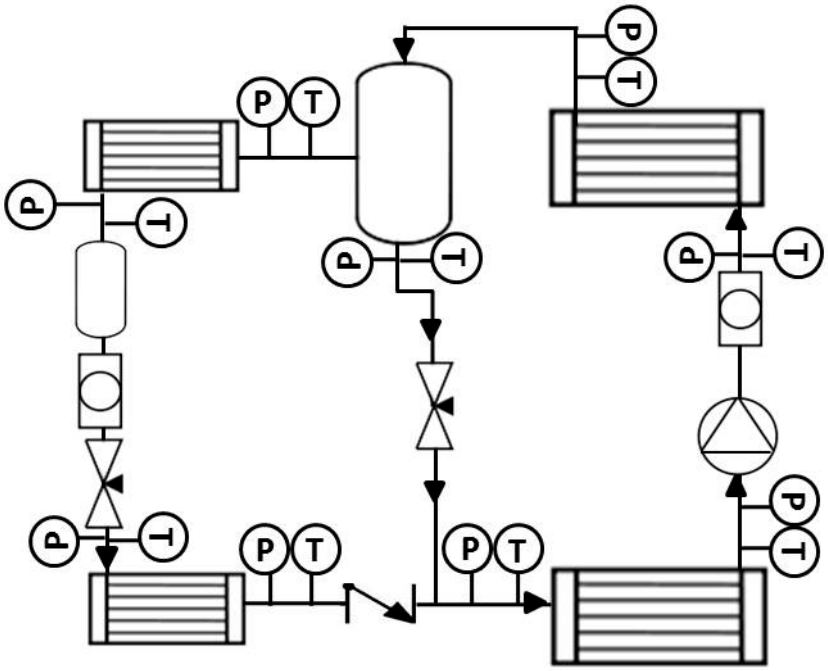

Figure 8.2: Schematic diagram of the experimental absorption system.

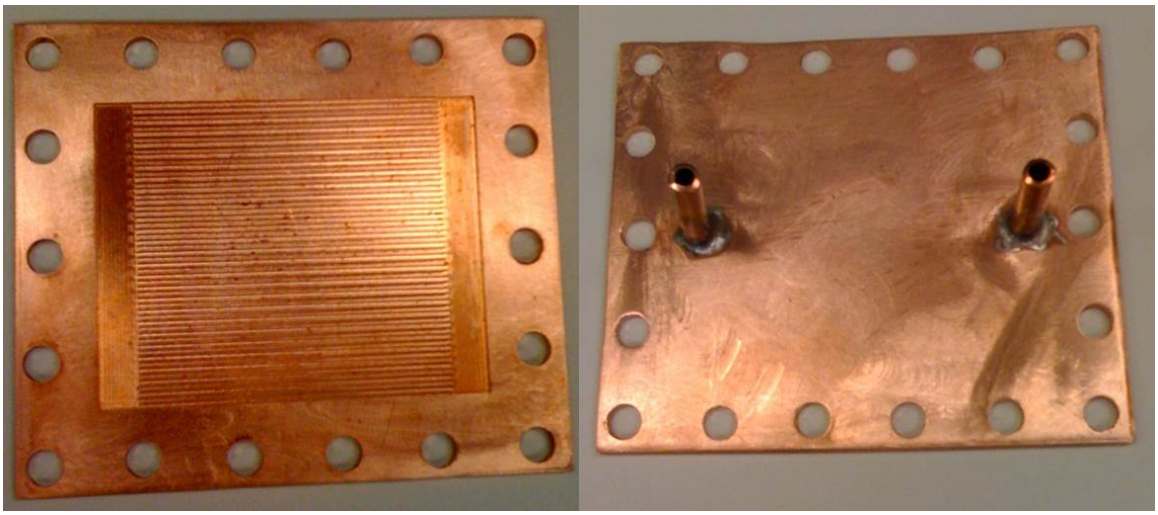

Figure 8.3: Absorber microchannels and cover plate with inlet and outlet ports.

To investigate the effect of desorber power (waste heat) input on the evaporator cooling capacity, the desorber power has been increased up to ~200 W to keep the evaporator temperature constant at 42^{o}C with the condenser and absorber coolant (secondary fluid) inlet temperatures of 22^{o}C. In addition, the effects of absorber and condenser coolant inlet temperatures were also investigated by varying both coolant inlet temperatures between 30^{o}C and 45^{o}C with the desorber power maintained at 120 W. The measured parameters were temperature, absolute pressure and electrical power input. The uncertainty in the temperature reading was 0.1K for the calibrated thermocouples relative to each other. The uncertainty in absolute pressure measurement was 0.25% of the maximum range of 2068 kPa (300 psi). The uncertainty in the output value of the electrical power transducer is given as 0.14% of the measured value. The heat transfer at the evaporator, Q_e, and desorber, Q_d, were measured in the experimental setup. The ratio of Q_e/Q_d is defined here as CE_{Th} which is the same as CE in Equation 2.13 except from the fact that the liquid pump work has been neglected, giving Equation 8.1.

$$\mathrm{CE}_{Th} = \frac{Q_e}{Q_d} \tag{8.1}$$

The pumping work was neglected in Equation 8.1 because the experimental system was not designed for efficient pumping due to the excessive use of sensors and piping. In addition, the pumping work (W_p) is usually about two orders of magnitude smaller than the heat terms, therefore, CE_{Th} is often interchangeably used with CE. Applying error propagation analysis to Equation 8.1 gives the estimated uncertainty of 0.2%. Two types of IL based working fluids were tested in the bench-top absorption refrigeration test system: R134a/[bmim][PF_6] and R134/[bmim][PF_6].

8.2 Experimental and Material Selection

The ionic liquid [bmim][PF_6] (iolitec, 99%), R134 (SynQuest Laboratory, Inc., 98%), and R134a (Airgas, 99.9%) were used as received. When the refrigerant was changed from R134a to R134, the R134a was discharged from the bench top system using a refrigerant recovery unit. A port on the refrigerant loop prevented drainage of the ionic liquid. The presence of a check valve and vertical cylinder between the solution loop and refrigerant loop also worked as a barrier for ionic liquid overflow. The [bmim][PF_6] in the system remained under vacuum for several days until there was no further change in the pressure. R134 was then loaded into the system to the same level as R134a as determined by the saturated pressure.

8.3 Results and Discussion

8.3.1 R134a/[bmim][PF_6]

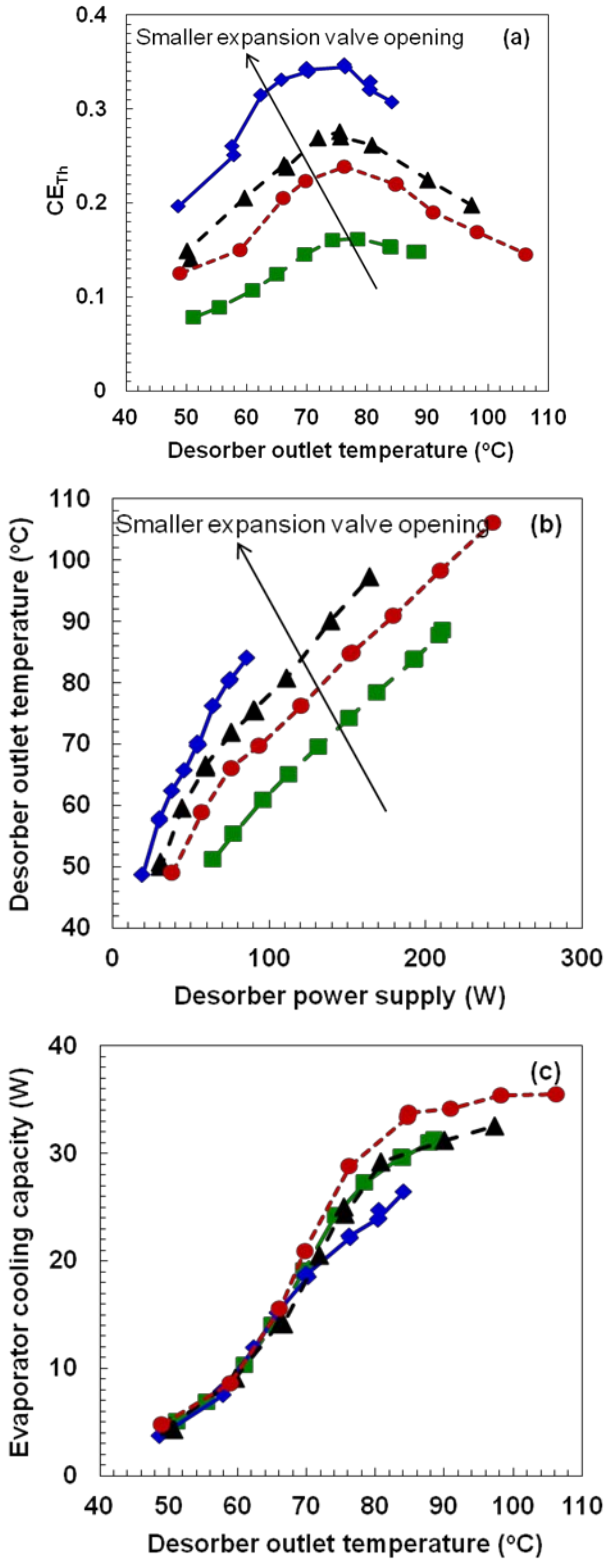

Figure 8.4: Experimentally measured (a) CE_{Th} and (c) evaporator cooling capacity with respect to the desorber outlet temperature and (b) the relation between the desorber outlet temperature and desorber power input.

Figure 8.4(a) shows the experimentally measured CE_{Th} of the absorption refrigeration system using R134a/[bmim][PF_6] mixture as the working fluid pair. Similar to the predictions in Figures 5.2 and 5.3, the CE_{Th} values were from 0.1 to 0.4 without a solution heat exchanger. Also, the system performance reached its maximum at the desorber outlet temperatures around 75^{o}C to 80^{o}C,where the range of the temperatures is consistent with the theoretical results shown in Figure 5.2. Considering that practical imperfections of the system as well as the fact that the details of heat/mass exchange processes in the system components have not been fully reflected in the model, the system-level predictions are in fairly good agreement with the experimental data. It is observed that with the smaller solution expansion valve opening, the system showed better performance (Figure 8.4(a)). This is because less desorber power (Q_d) is consumed with the narrowed solution expansion valve flow path which brings about the reduced solution flow rate (Figure 8.4(b)). The evaporator cooling capacity increased with increasing desorber outlet temperature (Figure 8.4(c)), due to the larger solubility difference between the weak and strong IL solution. However, as the desorber outlet temperature increased, the circulation ratio was reduced because the decrease in x_s becomes insignificant, which results in the saturation of the evaporator cooling capacity enhancement in Figure 8.4(c). Therefore, trial and error operation at different system conditions was necessary to find the optimum operating condition, especially when waste heat was used.

Figure 8.5 shows the effect of the refrigerant inlet temperature variation on the system performance. The absorber outlet temperature changed approximately proportional to the inlet of the absorber coolant temperature (Figure 8.5(a)). When the

coolant inlet temperature varied in the range of 23^{o}C to 39^{o}C, the absorber outlet temperature of the working fluid solution varied between 30^{o}C and 44^{o}C. Both the CE_{Th} and evaporator cooling capacity decrease with increasing absorber outlet temperature, which is attributed to the increase of circulation ratio due to the decrease of the refrigerant mole fraction, x_w in the weak-IL solution.

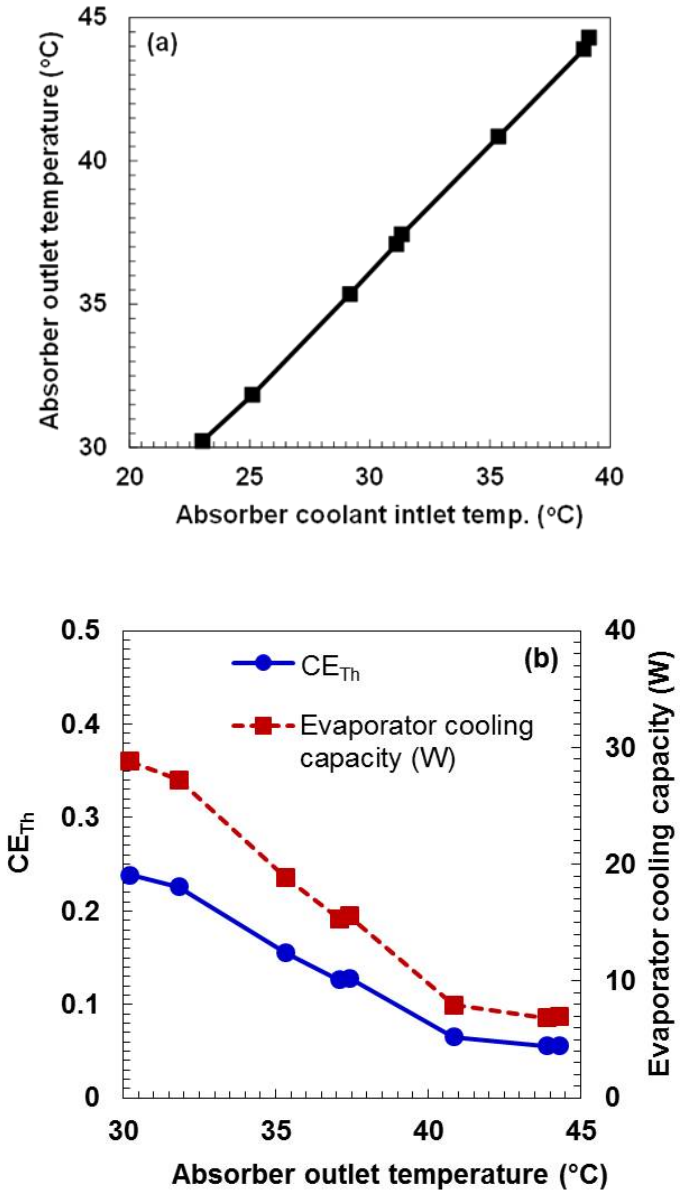

Figure 8.5: Experimentally measured (a) relation between the absorber outlet temperature and the absorber coolant inlet temperature and (b) CE_{Th} with respect to the absorber outlet temperature.

8.3.2 R134/[bmim][PF_6]

The evaporator junction temperature, which reflects the operating temperature of an electronic device or other component requiring cooling, was maintained to be at 42°C by controlling the heater power at the evaporator. Data were collected at different desorber temperatures by adjusting the heater power attached to the desorber. The desorber outlet temperature was measured prior to the separation of the refrigerant vapor produced. That is, it is an IL-vapor mixture combining states 3 and 8 in Figure 2.2. The evaporator junction temperature, evaporator outlet fluid temperature, separator outlet fluid temperature (state 8 in Figure 2.2), and desorber outlet fluid temperature at specific desorber power values are shown in Figure 8.6. The increase in the solution leaving the separator and desorber temperature is an expected result. The evaporator outlet temperature decreased with respect to the desorber heater power because of the overall increased pressure values in the system resulting from the higher desorber fluid temperature, which in turn results in a lower vaporization temperature for the refrigerant. The same trends were obtained for R134a/[bmim][PF_6] working fluids.

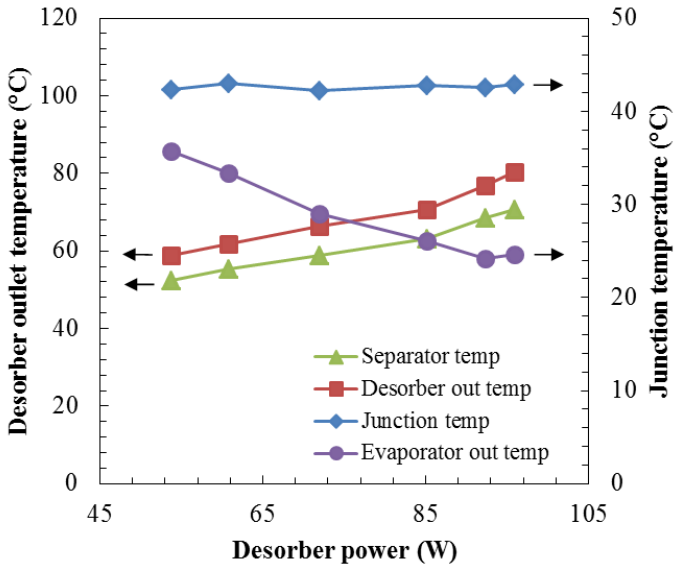

Figure 8.6: Experimentally measured desorber outlet fluid temperature, separator outlet fluid temperature, evaporator junction temperature, and evaporator outlet temperature with respect to desorber power input for R134/[bmim][PF_6] working fluid.

The CE under the operating conditions of Figure 8.6 had a local maximum, Figure 8.7, as predicted by the computational analysis due to the tradeoff between the desorber heater power and the cooling occurring at the evaporator. The experimental R134/[bmim][PF_6] efficiency values were smaller than the theoretical values, Figure 6.3, due to experimental losses in heat at various locations. The experimental bench-top system was insulated but not optimized. The temperature and pressure sensors and excess piping added to accommodate their installation made the system larger and less insulated than an optimized system. In addition, the performance can be improved by adding a solution heat exchanger and improving the design of the microchannel absorber and desorber. Also the theoretical results were computed to give the maximized values under a certain operating condition whereas the experimental system depends highly on fluid flowrates (Figure 8.5). Nevertheless, the experimental system results proved that the

performance trends predicted by simulations were correct and that a fluorocarbon/IL refrigerant pair can be made into a working system.

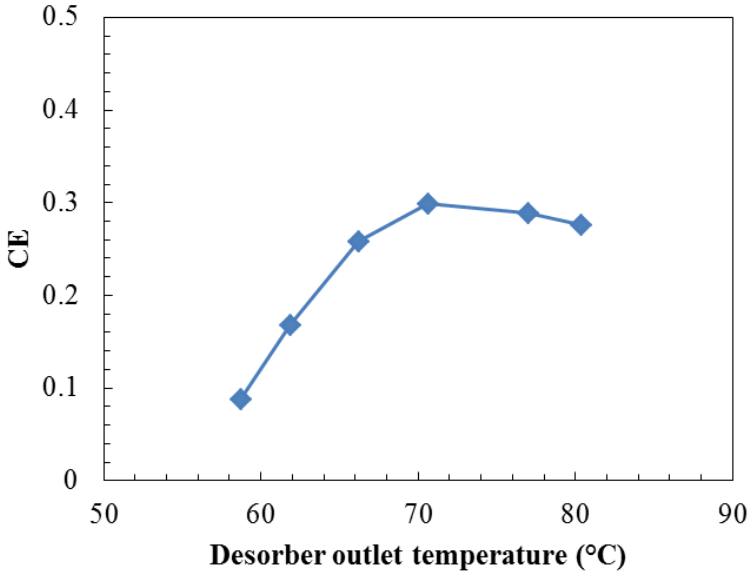

Figure 8.7: Experimentally measured CE_{Th} for R134/[bmim][PF_6] working fluid with respect to desorber outlet fluid temperature.

8.3.3 R134a and R134 Refrigerant Comparison

The cooling capacity of the R134/IL was also collected while measuring the CE values shown in Figure 8.7. The results were compared with that of R134a/IL working which were operated under nearly the same operating conditions and same amount of [bmim][PF_6], Figure 8.8. The R134/IL pair reached its maximum cooling capacity at a relatively low separator temperature of 63.26°C. This is 1.9 times larger than that of the R134a/IL working pair. Therefore, the R134/IL pair forms a highly effective working fluid pair for recycling low grade waste heat. The results are in good agreement with the

EOS model when the measured temperature and pressure values are given as input parameters. The EOS model calculations show that R134/IL is predicted to have 1.82 times larger cooling capacity than that of R134a/IL which is very close to the measured values.

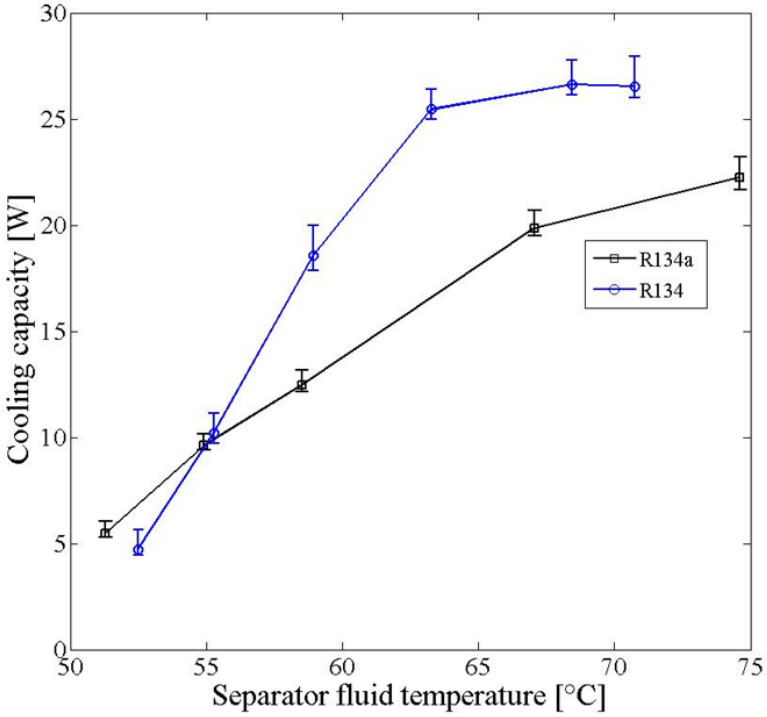

Figure 8.8: Comparison of experimental cooling capacity between R134/[bmim][PF_6] and R134a/[bmim][PF_6] working fluid pairs.

8.4 Conclusion

A laboratory scale experimental setup for the absorption heat pump system using R134a/[bmim][PF_6] and R134/[bmim][PF_6] mixtures as working fluids has been built to evaluate the feasibility of the system. With the desorber outlet temperature ranging from 50 to 110^{o}C, the R134a/[bmim][PF_6] system was operated with the maximum CE_{Th} of 0.35 and evaporator cooling capacity of 36 W without a solution heat exchanger. Experimental results confirmed the larger cooling capacity of the R134/[bmim][PF_6] working fluid pair than the R134a /[bmim][PF_6] pair. The maximum cooling capacity of R134/[bmim][PF_6] working fluid pair was reached at a relatively low separator fluid temperature (63.26°C), which would allow more effective waste heat utilization. Considering that practical imperfections of the system as well as the details of heat/mass exchange processes in the system components have not been fully reflected in the model, the system-level predictions are in fairly good agreement with the experimental data. With the addition of a solution heat exchanger and adjustment of the operating conditions, significant improvement of CE is expected as predicted from the theoretical simulations.

CHAPTER 9

SUMMARY AND CONCLUSIONS

In this research, the feasibility of ILs as a new absorbent in absorption refrigeration systems has been investigated. Various refrigerants and ILs have been studied. With full utilization of waste heat, the COP of an absorption heat pump using R134a/[bmim][PF_6] was nearly 20 times of that of a vapor compression system using R134a refrigerant and 50 times higher than that of commercial absorption refrigeration systems at moderate desorber and absorber temperatures of 80°C and 36.5°C, respectively. Therefore, the introduction of an IL based absorption system will contribute in significant cost savings in energy intensive buildings such as data centers.

The RK-EOS-two phase pressure drop model used in this work show close predictions of the experimental results in terms of cooling capacity of specific working fluid systems and temperature ranges that give maximum system efficiency. Among the studied HFC refrigerants and IL absorbents, the R134/[bmim][PF_6] working fluid pair showed the highest efficiency with CE of 0.67 and COP of 280 at desorber and absorber temperatures of 65°C and 27.5°C, respectively. The CE values can be further improved by changing the operating temperatures and introducing a solution heat exchanger.

Several working fluid selection criteria can be drawn by comparing the efficiency of various mixtures studied in this work: (1) the refrigerant should have high solubility in the absorbent; (2) the affinity between the refrigerant and absorbent should greatly depend on temperature; (3) the operating pressure of the refrigerant should be small. The current system model provides useful insight into the working fluids and the operating

conditions. A more detailed model would be beneficial for understanding/characterizing the effects of flow mal-distributions in microfluidic channel, kinetics of absorption/desorption processes, liquid-vapor separations, and heat exchanger effectiveness.

An IL based bench-top absorption system was built and operated for the first time. Both R134a and R134 refrigerants were paired with absorbent [bmim][PF_6] which were tested in the system. R134 showed 1.9 times higher cooling capacity than that of R134a at a moderate desorber outlet temperature of 63.26°C when the same amount of absorbent was used. Results show that the IL/HFC pairs showed sufficient cooling in a simple configuration hand built absorption system which demonstrates the feasibility as promising working fluids that can replace NH_3/H_2O and H_2O/LiBr systems.

Operation of the prototype test set up was successful, but there is plenty of room for further improvements. Future studies on the system performance optimization, introduction of a solution heat exchanger, and more efficient absorber and desorber designs are suggested. A study based on pumping work optimization should also be investigated to maximize the COP.

Finally, for practical implementation of ILs in the absorption systems, the complimentary studies concerning the detailed effects of heat and mass transfer characteristics and geometries of heat/mass exchangers are needed. Also, optimal microfluidic absorber and desorber configurations need to be developed to fully realize the promising potential of an absorption refrigeration system based on the IL chemical compressor.

REFERENCES

(1) Brown, R.; Nordman, B.; Tschudi, B.; Shehabi, A.; Stanley, J.; Koomey, J.; Sartor, D.; Chan, P.; Loper, J.; Capana, S.; Hedman, B.; Duff, R.; Haines, E.; Sass, D.; Fanara, A. *Report to Congress on Server and Data Center Energy Efficiency—Public Law 109-431*; Lawrence Berkeley National Laboratory, 2008.

(2) Greenberg, S.; Mills, E.; Tschudi, B.; Rumsey, P.; Myatt, B. In *Proceeding of the ACEEE Summer Study on Energy Efficiency in Buildings*; Asilomar, CA, 2006; pp. 76–87.

(3) Pakbaznia, E.; Pedram, M. In *2009 ACM/IEEE International Symposium on Low Power Electronics and Design, ISLPED'09, August 19, 2009 - August 21, 2009*; Institute of Electrical and Electronics Engineers Inc.: San Fancisco, CA, United states, 2009; pp. 145–150.

(4) Bansal, P. K.; Martin, A. *Int. J. Energy Res.* **2000**, *24*, 93–107.

(5) Srikhirin, P.; Aphornratana, S.; Chungpaibulpatana, S. *Renew. Sustain. Energy Rev.* **2001**, *5*, 343–372.

(6) Rosenquist, G.; McNeil, M.; Iyer, M.; Meyers, S.; McMahon, J. *Energy Policy* **2006**, *34*, 3257–3267.

(7) Shiflett, M. B.; Yokozeki, A. Absorption cycle utilizing ionic liquid as working fluid. WIPO Patent No.2006084262, 2006.

(8) Wasserscheid, P.; Keim, W. *Angew. Chem. Int. Ed. Engl.* **2000**, *39*, 3772–3789.

(9) Schaefer, L. *Ph.D. thesis, Georg. Inst. Technol.* **2000**.

(10) Herold, K. E.; Radermacher, R.; Klein, S. A. *Absorption chillers and heat pumps*; CRC Press: Boca Raton, FL, 1996; p. 329 p.

(11) Anderson, O. E. *Refrigeration in America: a history of a new technology and its impact*; Port Washington, N.Y., Kennikat Press, 1972.

(12) Berestneff, A. A. Absorption refrigeration system. U.S. Patent No. 2,565,943, 1951.

(13) Heintz, A.; Lehmann, J. K.; Wertz, C. *J. Chem. Eng. Data* **2003**, *48*, 472–474.

(14) Scammells, P. J.; Scott, J. L.; Singer, R. D. Ionic Liquids: The Neglected Issues. *Aust. J. Chem.* **2005**, *58* , 155–169.

(15) Wilkes, J. S. *J. Mol. Catal. A Chem.* **2004**, *214*, 11–17.

(16) Hagiwara, R.; Ito, Y. *J. Fluor. Chem.* **2000**, *105*, 221–227.

(17) Blake, D. M.; Moens, L.; Rudnicki, D.; Pilath, H. *J. Sol. energy Eng.* **2006**, *128*, 54–57.

(18) Cull, S. G.; Holbrey, J. D.; Vargas-Mora, V.; Seddon, K. R.; Lye, G. J. *Biotechnol. Bioeng.* **2000**, *69*, 227–233.

(19) Huddleston, J. G.; Willauer, H. D.; Swatloski, R. P.; Visser, A. E.; Rogers, R. D. *Chem. Commun.* **1998**, 1765–1766.

(20) Swatloski, R. P.; Spear, S. K.; Holbrey, J. D.; Rogers, R. D. *J. Am. Chem. Soc.* **2002**, *124*, 4974–4975.

(21) Smiglak, M.; Reichert, W. M.; Holbrey, J. D.; Wilkes, J. S.; Sun, L.; Thrasher, J. S.; Kirichenko, K.; Singh, S.; Katritzky, A. R.; Rogers, R. D. *Chem. Commun. (Camb).* **2006**, 2554–2556.

(22) Jastorff, B.; Störmann, R.; Ranke, J.; Mölter, K.; Stock, F.; Oberheitmann, B.; Hoffmann, W.; Hoffmann, J.; Nüchter, M.; Ondruschka, B.; Filser, J. *Green Chem.* **2003**, *5*, 136–142.

(23) Rogers, R. D.; Seddon, K. R. *Sci.* **2003**, *302* , 792–793.

(24) Dzyuba, S. V; Bartsch, R. A. *ChemPhysChem* **2002**, *3*, 161–166.

(25) Marsh, K. N.; Boxall, J. A.; Lichtenthaler, R. *Fluid Phase Equilib.* **2004**, *219*, 93–98.

(26) Troncoso, J.; Cerdeiriña, C. A.; Sanmamed, Y. A.; Romaní, L.; Rebelo, L. P. N. *J. Chem. Eng. Data* **2006**, *51*, 1856–1859.

(27) Valkenburg, M. E. V.; Vaughn, R. L.; Williams, M.; Wilkes, J. S. *Thermochim. Acta* **2005**, *425*, 181–188.

(28) Huddleston, J. G.; Visser, A. E.; Reichert, W. M.; Willauer, H. D.; Broker, G. A.; Rogers, R. D. *Green Chem.* **2001**, *3*, 156–164.

(29) Mclinden, M.; Klein, S.; Lemmon, E.; Peskin, A. NIST thermodynamic and transport properties of refrigerants and refrigerant mixtures database (REFPROP). Version 6.0 **1998**.

(30) Welty, J. R. *Fundamentals of momentum, heat, and mass transfer*; 4th ed.; Wiley: New York, 2001; p. xii, 759 p.

(31) Smith, J. M.; Van Ness, H. C.; Abbott, M. M. *Introduction to chemical engineering thermodynamics*; 7th ed.; McGraw-Hill: Boston, 2005; p. xviii, 817 p.

(32) Shiflett, M. B.; Yokozeki, A. *AIChE J.* **2006**, *52*, 1205–1219.

(33) Yokozeki, A.; Sato, H.; Watanabe, K. *Int. J. Thermophys.* **1998**, *19*, 89–127.

(34) Yokozeki, A. *Appl. Energy* **2005**, *80*, 383–399.

(35) Yokozeki, A. *Int. J. Thermophys.* **2001**, *22*, 1057–1071.

(36) Yokozeki, A.; Shiflett, M. B. *Ind. Eng. Chem. Res.* **2010**, *49*, 9496–9503.

(37) Jacquemin, J.; Husson, P.; Padua, A. A. H.; Majer, V. *Green Chem.* **2006**, *8*, 172–180.

(38) Carey, V. P. *Liquid-vapor phase-change phenomena : an introduction to the thermophysics of vaporization and condensation processes in heat transfer equipment*; Hemisphere Pub. Corp.: Washington, D.C., 1992; p. xvii, 645 p.

(39) Kim, Y. J.; Joshi, Y. K.; Fedorov, A. G. An absorption based miniature heat pump system for electronics cooling. *Int. J. Refrig.* **2008**, *31*, 23–33.

(40) Lockhart, R. W.; Martinelli, R. C. *Chem. Eng. Prog.* **1949**, *45*, 39–45.

(41) Lee, J.; Mudawar, I. *Int. J. Heat Mass Transf.* **2005**, *48*, 928–940.

(42) Shah, R. K.; London, A. L. *Advances in heat transfer: Supplement*; Academic Pr, 1978; Vol. 1.

(43) Zivi, S. M. *J. Heat Transfer* **1964**, *86*, 247.

(44) Sharma, P.; Park, S. Do; Baek, I. H.; Park, K. T.; Yoon, Y. I. I.; Jeong, S. K. *Fuel Process. Technol.* **2012**, *100*, 55–62.

(45) http://www.engineeringtoolbox.com/Refrigerants-Environment-Properties-d_1220.html.

(46) Budzianowski, W.; Koziol, A. *Chem. Eng. Res. Des.* **2005**, *83*, 196–204.

(47) Ren, W.; Scurto, A. M. *Fluid Phase Equilib.* **2009**, *286*, 1–7.

(48) Shiflett, M. B.; Yokozeki, A. *J. Chem. Eng. Data* **2007**, *52*, 2007–2015.

(49) Kato, R.; Gmehling, J. *Fluid Phase Equilib.* **2005**, *231*, 38–43.

(50) Seiler, M.; Jork, C.; Kavarnou, A.; Arlt, W.; Hirsch, R. *AIChE J.* **2004**, *50*, 2439–2454.

(51) Gardas, R. L.; Coutinho, J. A. P. *AIChE J.* **2009**, *55*, 1274–1290.

(52) Gardas, R. L.; Coutinho, J. a. P. *Ind. Eng. Chem. Res.* **2008**, *47*, 5751–5757.

(53) Jacquemin, J.; Husson, P.; Mayer, V.; Cibulka, I. *J. Chem. Eng. Data* **2007**, *52*, 2204–2211.

(54) Aki, S. N. V. K.; Mellein, B. R.; Saurer, E. M.; Brennecke, J. F. *J. Phys. Chem. B* **2004**, *108*, 20355–20365.

(55) Kerlé, D.; Ludwig, R.; Geiger, A.; Paschek, D. *J. Phys. Chem. B* **2009**, *113*, 12727–12735.

(56) Hildebrand, J.; Scott, R. *Regular solutions*; Prentice Hall: Englewood Cliffs, NJ, 1962.

(57) Prausnitz, J. M. *AIChE J.* **1958**, *4*, 269–272.

(58) Anthony, J. L.; Maginn, E. J.; Brennecke, J. F. *J. Phys. Chem. B* **2001**, *105*, 10942–10949.

(59) Finotello, A.; Bara, J. E.; Camper, D.; Noble, R. D. *Ind. Eng. Chem. Res.* **2008**, *47*, 3453–3459.

(60) LaFrate, A. L.; Bara, J. E.; Gin, D. L.; Noble, R. D. *Ind. Eng. Chem. Res.* **2009**, *48*, 8757–8759.

(61) Nie, N.; Zheng, D.; Dong, L.; Li, Y. *J. Chem. Eng. Data* **2012**, *57*, 3598–3603.

(62) Yokozeki, A.; Shiflett, M. B. *AIChE J.* **2006**, *52*, 3952–3957.

(63) Aphornratana, S.; Sriveerakul, T. *Exp. Therm. Fluid Sci.* **2007**, *32*, 658–669.

(64) Shiflett, M. B.; Yokozeki, A. *Ind. Eng. Chem. Res.* **2006**, *45*, 6375–6382.

(65) Calculated using Advanced Chemistry Development (ACD/Labs) Software V11.02 (© 1994-2013 ACD/Labs).

(66) Maezawa, Y.; Sato, H.; Watanabe, K. *J. Chem. Eng. Data* **1991**, *36*, 151–155.

(67) Muldoon, M. J.; Aki, S. N. V. K.; Anderson, J. L.; Dixon, J. K.; Brennecke, J. F. *J. Phys. Chem. B* **2007**, *111*, 9001–9009.

(68) Shiflett, M. B.; Yokozeki, A. *J. Phys. Chem. B* **2007**, *111*, 2070–2074.

(69) Harrison, B. K.; Seaton, W. H. *Ind. Eng. Chem. Res.* **1988**, *27*, 1536–1540.

(70) Ahosseini, A.; Scurto, A. M. *Int. J. Thermophys.* **2008**, *29*, 1222–1243.

(71) Shiflett, M. B.; Yokozeki, A. *Fluid Phase Equilib.* **2007**, *259*, 210–217.